Available online at www.sciencedirect.com
SCIENCE DIRECT
Icarus 172 (2004) 479–502
ICARUS
www.elsevier.com/locate/icarus

Numerical modeling of ionian volcanic plumes with entrained particulates

J. Zhang *, D.B. Goldstein, P.L. Varghese, L. Trafton, C. Moore, K. Miki

Department of Aerospace Engineering, The University of Texas at Austin, 1 University Station, C0600, Austin, TX 78712-0235, USA

Received 18 November 2003; revised 27 May 2004

Available online 12 September 2004

Abstract

Volcanic plumes on Jupiter's moon Io are modeled using the direct simulation Monte Carlo (DSMC) method. The modeled volcanic vent is interpreted as a "virtual" vent. A parametric study of the "virtual" vent gas temperature and velocity is performed to constrain the gas properties at the vent by observables, particularly the plume height and the surrounding condensate deposition ring radius. Also, the flow of refractory nano-size particulates entrained in the gas is modeled with "overlay" techniques which assume that the background gas flow is not altered by the particulates. The column density along the tangential line-of-sight and the shadow cast by the plume are calculated and compared with Voyager and Galileo images. The parametric study indicates that it is possible to obtain a unique solution for the vent temperature and velocity for a large plume like Pele. However, for a small Prometheus-type plume, several different possible combinations of vent temperature and velocity result in both the same shock height and peak deposition ring radius. Pele and Prometheus plume particulates are examined in detail. Encouraging matches with observations are obtained for each plume by varying both the gas and particle parameters. The calculated tangential gas column density of Pele agrees with that obtained from HST observations. An upper limit on the size of particles that track the gas flow well is found to be ~ 10 nm, consistent with Voyager observations of Loki. While it is certainly possible for the plumes to contain refractory dust or pyroclastic particles, especially in the vent vicinity, we find that the conditions are favorable for SO_2 condensation into particles away from the vent vicinity for Prometheus. The shadow cast by Prometheus as seen in Galileo images is also reproduced by our simulation. A time averaged frost deposition profile is calculated for Prometheus in an effort to explain the multiple ring structure observed around the source region. However, this multiple ring structure may be better explained by the calculated deposition of entrained particles. The possibility of forming a dust cloud on Io is examined and, based on a lack of any such observed clouds, a subsolar frost temperature of less than 118 K is suggested.

Keywords: Satellites of Jupiter; Io; Atmospheres, dynamics; Volcanism

1. Introduction

Our understanding of Io's atmosphere has improved substantially due to recent observations and theoretical analyses. The importance of the role of volcanoes in generating and maintaining Io's SO_2 atmosphere has been emphasized. Strobel and Wolven (2001) found that only eight Pele-type volcanoes would be needed to account for the SO_2 abundance inferred from reflected solar Lyman-α intensity data. Thus, they suggested that, in addition to a sublimation atmosphere, volcanic plume atmospheres may also contribute substantially to the overall atmosphere. Recently, we compared the vertical column density of SO_2 from modeled day/night side Pele-type plumes and an undisturbed sublimation atmosphere, and found that plume atmospheres play a role as concentrated perturbations of the sublimation atmosphere near the plume axis. An observation spatial resolution better than 30 km is needed to detect the maximum column density near the plume axis within a sublimation atmosphere (Zhang et al., 2003a). Thus, a smooth SO_2 distribution based on a lower spatial resolution observations should not be taken as the evidence of the absence of volcanic atmospheres. In an effort to explain the presence of alkali and halogen species in the atmosphere, Moses et al. (2002) used a one-dimensional model includ-

* Corresponding author. Fax: 773-834-3230.
E-mail address: zhang@flash.uchicago.edu (J. Zhang).

0019-1035/$ – see front matter
doi:10.1016/j.icarus.2004.06.016

ing chemical kinetics and diffusion to simulate the photochemical processing in Pele's volcanic gas. Lellouch et al. (2003) also investigated the possibility of volcanically emitted sodium chloride as a source for Io's neutral clouds and plasma torus, and suggested that the volcanic emissions provide important sources of Na and Cl. Dynamic volcanic plume models are essential to efforts to link the plumes to the various observations mentioned above. However, such dynamic models are quite complex (Kieffer, 1982; Lellouch, 1996). Various models from Stochastic–Ballistic to computational fluid dynamics (CFD) to rarefied gas dynamics have been developed and adopted for dynamical studies of volcanoes as summarized recently by Douté et al. (2002). Unfortunately, these models are physically different and sometimes internally inconsistent. The Stochastic–Ballistic (SB) model can satisfactorily reproduce the plume shape and ring deposition of some plumes by careful manipulation of the initial conditions. However, the thermal motion of individual particles and their collisions are not taken into account in a SB model so that the resulting flow field does not reflect features such as shocks or the acceleration and cooling of the gas through expansions which should occur at certain locations. We believe that the SB model is not suitable for the simulation of the gas flow, and the constraints it places on the initial conditions are not accurate. Continuum flow models have limited applicability because of the wide-range of flow regimes occurring in plumes. Conditions range from a virtually continuum flow close to the vent to free-molecular flow far from it. The continuum assumption breaks down in low-density flows because the mean free path of molecules becomes comparable to the length scale of flow features which invalidates the continuum flow approximations. The difficulties posed by the Stochastic–Ballistic and continuum flow models are overcome by the direct simulation Monte Carlo (DSMC) approach (Bird, 1994) which has been adopted and applied to volcanic plume modeling and sublimation driven flows by Austin and Goldstein (1995, 2000). We have followed this approach and developed our gas dynamic, radiation and gas/particulates flow model based on it (Zhang et al., 2001, 2003a, 2003b, 2003c; Moore et al., 2003).

Galileo observations have suggested that the magma temperature at Pele may exceed 1700 K (Lopes-Gautier et al., 2002). Zolotov and Fegley (2001) calculated a total vent pressure of 0.01 to 2 bar at a vent temperature of 1760 ± 210 K for Pele. These are drastically different from the vent conditions ($T = 650$ K and $P = 40$ nbar) that we used previously to reproduce the plume shape of Pele and the vertical column density observed around Pele (Zhang et al., 2003a). However, this large difference may be reconcilable if the precise definition of a "vent" is distinguished for the different studies. It is also important to determine whether the models reproduce the observations over a wider range of vent conditions, a byproduct of which would be a functional dependence of the plume shape on vent conditions. One may then be able to constrain the vent conditions by the plume shape. In this paper, a parametric study of the "virtual" vent conditions, specifically the vent temperature and velocity, is performed and a clarification of the definition (geometry and location) of the vent in our simulations is attempted. The concept of a "virtual" vent makes our simulation applicable to various types of possibly complex volcanic sources. In fact, the sources of volcanic eruptions on Io are quite complicated and at least three sources of vent material have been proposed for Prometheus: the interaction of flowing lava and preexisting volatile deposits on the surface, direct degassing from the lava, or the eruption of a liquid aquifer from underground (Douté et al., 2002).

Many ionian volcanoes manifest themselves by particulates rising high above the surface and many observable features of ionian volcanic plumes are associated with the fine particulates in these plumes. Most of the Voyager and Galileo plume images likely show sunlight reflected by particles (possibly snow-flakes, droplets and/or dust) entrained in the plumes. Photometric studies of Loki by Collins (1981) indicate that particles of various sizes (from 0.01 up to 1000 μm) are present. Strom and Schneider (1982) suggested that the bright envelope appearing in the smoothed ultraviolet brightness images of Pele may be the result of a concentration of particles at a shock front. The wavelength dependence of the optical depth in 1996 HST observations of Pele can be matched by either a plume of SO_2 gas having an average column density of $\sim 3.7 \times 10^{17}$ cm^{-2} or a plume of very small scattering particles with maximum size of 0.08 μm (Spencer et al., 1997). Thus, it is important to study the behavior of gas/particle flow in these volcanic plumes once the gas dynamic model has been developed; such a gas/particle flow model enables one to understand the observed plume images better. Meanwhile, the deposition patterns around Prometheus are among the most dramatic features on Io and have attracted much attention. Douté et al. (2002) obtained maps of SO_2 areal abundance and mean grain size around Prometheus, and used a semiempirical ballistic model to examine the progressive emplacement of the SO_2 ring. Geissler et al. (2003) suggested that there is a multiple ring structure around Prometheus with the radii of these ring deposits centered at 72 km (bright yellow), 95 km (dark), 125 km (white), and 200 km (a faint yellow ring that becomes prominent at high solar phase angles).

In this paper, we focus on the gas/particle flow in the volcanic plumes, and present and discuss promising matches to the Voyager plume images of Prometheus and Pele. We also present simulations of the ring deposition structure of gas or particles around Prometheus, and examine the possibility of duplicating the observed multiple ring structure. We first review and also introduce the new features of our DSMC model in Section 2. The method of parametric study, the "overlay" techniques used in the gas/particle flow modeling and the relevant issues are also described in Section 2. The results and comparisons, such as the matches to the plume images, plume shadows and deposition patterns, are introduced in Section 3. Section 4 contains the discussion of

the "virtual" vent concept, the lower bounding Mach number associated with a lava lake plume, the source of fine particulates in the plume and the constraints placed on the subsolar frost temperature.

2. Numerical method

A detailed discussion of the numerical method and previous results can be found in Zhang et al. (2003a, 2003b). An abbreviated discussion is provided here.

The Direct Simulation Monte Carlo (DSMC) method (Bird, 1994) was used to model the volcanic plume flows over a wide range of flow regimes, from a virtually continuum regime near the volcano vent to the free molecular regime at high altitude, with transitional flow in between. In DSMC the flow is represented by a large number of simulated particles which are moved and collided. The collisions between particles are simulated stochastically based on the kinetic theory of a dilute gas rather than deterministically as in molecular dynamics. Flow properties such as temperature and density are extracted by sampling and averaging over all the molecules. The innovations we have incorporated in our DSMC method include the inclusion of spherical geometry, a body force (gravity), SO_2 internal energy exchange, radiation from rotational lines[1] and discrete vibrational bands (aimed at connecting the gas dynamic simulation to the radiation signature of the plumes by remote sensing), multi-domain calculations to resolve radiation in the vent vicinity, and "overlay" gas/particle flow modeling. The model has reproduced the observed plume shape, ring deposition and some other features, and appears to be reasonably successful in simulating the plume flow and matching observations (Zhang et al., 2003a, 2003b). Additional encouraging matches have been found recently and will be shown in the Results section. We begin by briefly reviewing the flow conditions used in our simulations and then discuss the process of our parametric study and the gas/particle flow modeling in greater detail.

2.1. Review of flow conditions

The schematic diagram in Zhang et al. (2003a) is reproduced in Fig. 1 to illustrate the flow conditions and DSMC procedure used. To summarize, the flow is assumed to be axisymmetric and emerging at a uniform mean upward velocity (V_v) from a circular vent centered at the origin of the symmetry axis. The molecules also have random thermal velocities sampled from a Maxwellian distribution at the vent temperature (T_v), and carry equilibrium rotational and discrete vibrational energy. As will be discussed in Section 4, the vent in our simulation is interpreted as the "virtual" (or "effective") vent which represents the location where the gas

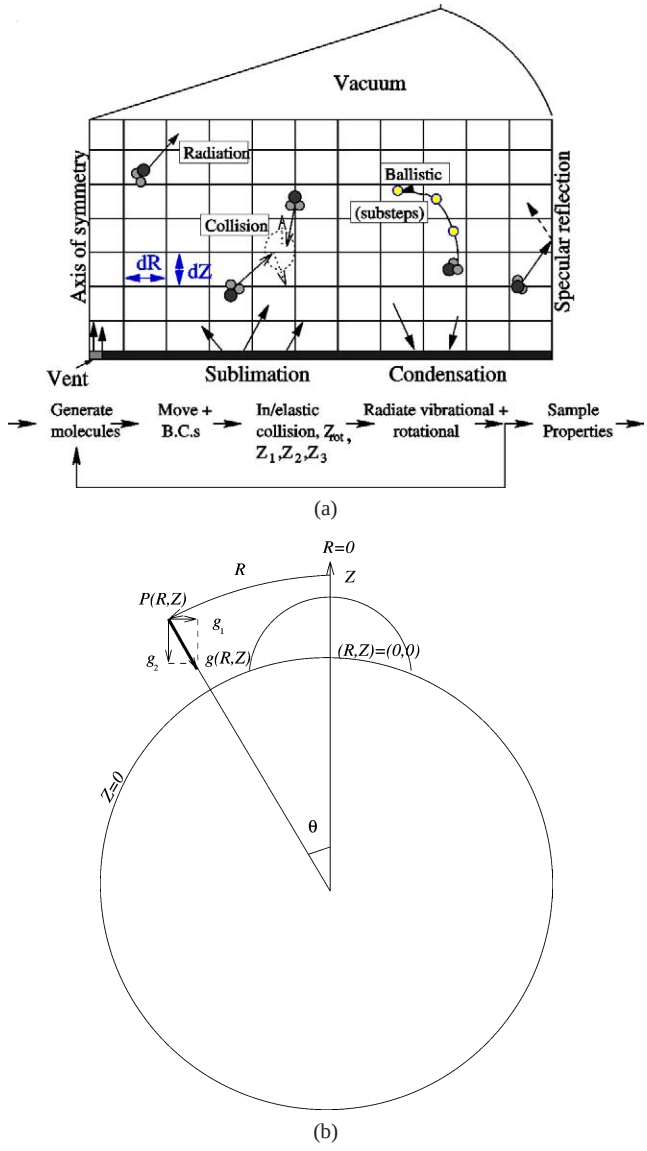

Fig. 1. Schematic of flow conditions and DSMC procedure in the simulation.

temperature and velocity reach the modeled values. Therefore, our virtual vent is not necessarily right at the exit of a volcanic tube and may apply to plumes having a lava-frost interaction as the source. The nominal vent radius is ~ 8 km. The effects of vent size are examined in Zhang et al. (2003c), Zhang (2004). Also, note that because the geometry of the conduit is unknown and because of the presumably complex expansion from the actual exit to the virtual vent (beyond the scope of this paper), the V_v and T_v at the virtual vent are uncorrelated. This is different from an assumption of isentropic expansion from specified reservoir conditions.

In early work (Zhang et al., 2003a, 2003b) a flat planet approximation was used. This is most appropriate for plumes that are small compared to the radius of Io. More recently, the spherical geometry was accounted for. The coordinates are interpreted in the manner shown in Fig. 1b. The altitude Z is interpreted as the distance from the spherical surface of

[1] The model for radiation from rotational lines is replaced by a classical model (Bird, 1994) in the present paper.

Io, and the radius R is interpreted as the length of the arc of a circle with origin at Io's center and a radius r of the distance from the point of interest to the center of Io ($R_0 + Z$), where $R_0 = 1800$ km is the radius of Io. The surface of Io corresponds to $Z = 0$ km, and the plume axis (also passing through the center of Io) corresponds to $R = 0$ km. The volume of each cell is $r^2 \sin(\theta)\, dr\, d\phi\, d\theta = r^2 \sin(\theta)\, dZ\, d\phi\, d\theta$, where θ is the zenith angle as indicated in Fig. 1b and equal to R/r, and $d\phi$ is set to unity. The gas is subject to Io's gravitational field after it erupts from the vent. The altitude- and direction-dependence of the gravitational acceleration has also been included.

The molecules escape into space if they cross the upper boundary of the computational domain (rarely), and are reflected by the outer specular wall when they collide with the circumferential boundary (but it is far away and does not alter the flows in the regions of interest). The surface of Io is assumed to be cold and very rough at the microscopic level and to have a sticking coefficient $\alpha = 1$, so the molecules condense if they contact the surface. Vapor also sublimes from the surface. Sublimated molecules are emitted randomly into a hemisphere at a rate specified by the equilibrium vapor pressure at the surface temperature.

Details of other recent innovations, such as the new model of vibration–translation energy exchange, and infrared and microwave emission from the gas, can be found in Zhang (2004).

2.2. Parametric study of vent conditions

Generally, the plume morphology (shape), the shock height, and the deposition pattern are all functions of the vent and surface conditions. A parametric study is performed for plumes assuming a surrounding surface temperature of 90 K. At such a low surface temperature, the sublimation atmosphere is negligible. Calculations show that a canopy shaped shock is generated in a volcanic gas plume as a result of the gas flow falling back on itself due to gravity, and a ring shaped deposition pattern is formed around the vent as the gas falls on the ground in a night side plume. As will be shown in Section 3.5.1, the diurnally averaged deposition profile has approximately the same peak deposition radius as that for nightside plume so the nightside deposition profile can be used to find the peak deposition radius. Also, the shock height is insensitive to the surface temperature. In fact, the canopy shock height is a good observable because of the concentration of particles at the shock whereas the plume summit is relatively fuzzy. Knowledge of the dependence of plume morphology on "virtual" vent[2] conditions is helpful in constraining those vent conditions using the observed plume shape. Quite often, the vent velocities are estimated by the ballistic height which is adequate for a zeroth order estimate. However, the ballistic estimate is not accurate when the thermal energy of the gas and intermolecular collisions in the gas contribute to the development of the plume shape (as will be shown by some examples in the Section 3). Hence, we carried out a parametric study on vent velocity (V_v) and temperature (T_v). Two sets of iso-contours in V_v–T_v space were mapped with one set corresponding to constant canopy shock heights (H_{shock}) and the other to constant peak deposition ring radii (R_{ring}). Since relatively simple contour shapes were expected, only sparsely distributed but carefully selected (V_v, T_v) points were examined. This reduced computational time compared to calculations on a closely spaced uniform (V_v, T_v) parameter grid. Iso-contours of H_{shock} (or R_{ring}) were obtained by interpolation in Tecplot (an engineering graphic software package), and relatively simple contour shapes were indeed observed. More accurate contours were then obtained by testing more (V_v, T_v) combinations as needed.

After these two sets of iso-contours were produced, we aimed to constrain the unique combination of the vent velocity and temperature by the observed shock height and peak deposition radius. It should be pointed out that the accuracy of the constraints depends on how good the model is and how well the assumptions at the vent represent reality. The assumptions here include an ~ 8 km "virtual" vent radius, a fixed source number density at the vent (5×10^{17} molecules/m^3), and an optically thin gas in the ν_1, ν_2, and ν_3 SO_2 vibrational bands. It will be shown in Section 3 that if the source number densities are changed within a certain range, the gas flows would still have nearly the same density contour shapes except that the contour levels would be scaled by the ratio of the two source number densities. For this reason, the source number density was kept fixed in the study. The assumption of optically thin gas at SO_2 vibrational bands is adequate if the "virtual" vent radius is ~ 8 km and the source number density is not too high. The opacity of the gas becomes significant and must be considered if the "virtual" vent radius is ~ 1 km and the source number density is high. However, as shown in Zhang et al. (2003c), the opacity of the gas generally causes only $\sim$ 10–20% differences in the constrained vent conditions. The accuracy of these assumptions will be discussed in greater detail in Section 4 after the results are presented.

2.3. "Overlay" gas/particle flow model

Special effort has been expended on modeling the gas/particle flow in these volcanic plumes. Spencer et al. (1997) showed that the wavelength dependence of the optical depth in 1996 HST observations of Pele can be matched by either a plume of SO_2 gas with a total mass of 1.1×10^{11} g or a dust plume of very small scattering particles with minimum total mass of 1×10^9 g and maximum particle sizes of 0.08 μm. They also suggested that either of these possibilities, or a combination of them, is consistent with Voyager and HST observations. Since there are many positive SO_2 gas detections (Sartoretti et al., 1996; Lellouch, 1996; McGrath et al., 2000) and Spencer et al. (1997) showed that

[2] The concept of "virtual" vent will be explained in Section 4.

their inferred SO_2 abundance is comparable to these estimates, it is reasonable to assume that Pele consists mainly of gas rather than dust, and the total mass of the gas is at least two orders of magnitude higher than dust. At such a low particle (dust) mass loading of less than $\sim 1\%$ it may be assumed that the flow of particles entrained in the gas plume does not alter the gas flow. Therefore, "overlay" techniques may be used to model the gas/particle flow.[3] Two "overlay" methods were used. In the first method, referred to as the Collision Model, the particles were treated simply as another molecular species in DSMC and were allowed to collide with gas molecules. These "molecules" are huge in size compared to gas molecules and collide elastically with the gas molecules. Since it is assumed that the particle flow does not alter the gas flow, only the particle velocities are modified by each collision that involves a gas molecule and a particle. Note that, in order to get a sufficiently smooth particle flow field, it is necessary to continue the computation of the steady background gas flow after the background gas flow reaches steady-state and the calculation of the particle flow started. The other method, referred to as the Drag Model, is to calculate the drag on the particles in a *precalculated* or frozen gas flow field and move the particles accordingly. Since the particle-size based Knudsen number, *Kn*, is much greater than one, the drag coefficient, C_d, in the free molecular limit (Eq. (1)) can be used (Bird, 1994):

$$C_d = \frac{(2s^2+1)\exp(-s^2)}{\sqrt{\pi}s^3} + \frac{(4s^4+4s^2-1)}{2s^4}\operatorname{erf}(s) + \frac{2(1-\varepsilon)\sqrt{\pi}}{3s}\left(\frac{T_w}{T_\infty}\right)^{1/2} \quad (1)$$

where, $s = U_\infty\beta_\infty = U_\infty/\sqrt{2kT/m}$, ε is the fraction of molecules that are reflected specularly (the remaining fraction $1-\varepsilon$ is reflected diffusely), T_w is the temperature of particles, and T_∞ is the temperature of the gas stream. Assuming a cold sphere or a fully specular reflection of molecules off the particles ($\varepsilon = 1$), the free-molecular drag coefficient is then reduced to the following,

$$C_d = \frac{(2s^2+1)\exp(-s^2)}{\sqrt{\pi}s^3} + \frac{(4s^4+4s^2-1)}{2s^4}\operatorname{erf}(s). \quad (2)$$

It is worth pointing out that one must be careful when dealing with small values of s: $C_d \to \frac{16}{3\sqrt{\pi}s}\exp(-s^2)$ as $s \to 0$. A very accurate value of π (at least 7–8 digits) should be used in Eq. (2) as $s \to 0$, otherwise the singular behavior of C_d will be incorrect and the finite drag ($\propto C_d s^2$) will become singular as $s \to 0$.

In both methods, it is assumed that the fine particulates are spherical (aimed at modeling crystals or droplets), and that the particle flow is so dilute that the particles do not collide with each other. The particles are released at zero velocity from the vent, although it should be recognized that the particles probably have an initial velocity. However, the effect of the initial velocity is small due to the close coupling between the motion of the gas and the nano-size particles that are the focus of the present work. The initial velocity is important if the particles are large (Zhang, 2004). In our models, the particles do undergo Brownian motion but it is not significant. The mean number density of the above mentioned 0.08 μm particles is ~ 8 orders of magnitude lower than the gas number density assuming dust particle mass loading of 1%. Thus, although the cross-sectional area of a particle is $\sim 10^4$ times larger than that of a gas molecule, the particle–particle collision frequency is still at least $\sim 10^4$ times lower than that of the gas molecules, and the assumption of no collisions between particles is thus justified. The particles are assumed to be *refractory* so that coagulation and evaporation are neglected in the models. The particles are also assumed to have a density of SO_2 liquid, 1.5 g/cm^3.

Each "overlay" method has computational advantages in different limits. The Collision Model is more suitable for nano-sized particles, while the Drag Model is best for relatively large, micron-sized particles. The collision rate of a nano-particle with the background gas molecules is not unreasonably large, thus the Collision Model is computationally affordable. Because of the large accelerations experienced by the nano-particles, the Drag Model requires an unreasonably small time step and thus is not suitable. For micron-particles, the collision rate with the background gas molecules becomes so large that the Collision Model is very expensive, but the particle trajectories can be easily computed by the Drag Model. Therefore, the Drag Model is used when particles are large, while the Collision Model is used if particles are small.

2.3.1. *Validation of the "Overlay" model*

The validation here relies on convergence studies. For the Collision Model, the "overlay" particle flow is expected to asymptotically approach the background gas flow if the particles have SO_2 molecular size and mass (thus virtual molecules). Such convergence has been obtained as shown in Fig. 2 which illustrates the number density contours of virtual SO_2 molecules and the background gas. Additionally, the Collision and Drag Models were run with identical particle sizes and the results agreed providing a measure of cross-validation. Figure 3 compares particle trajectories calculated with the Collision Model and the Drag Model for a few vent input locations for 10 nm particles.

2.3.2. *Collision weight*

As discussed above, the Collision Model is not suitable for the calculation of flows with large particles because the computation of the many collisions between a large particle and the background gas molecules becomes very time consuming. A "collision weight" can be used to extend the ability of the Collision Model to calculate flow of large particles. In such a calculation, the collision between a gas molecule and a particle is assumed to be N times as effective

[3] The fully coupled two-phase gas/particle flow has also been briefly examined using the DSMC method in Zhang (2004).

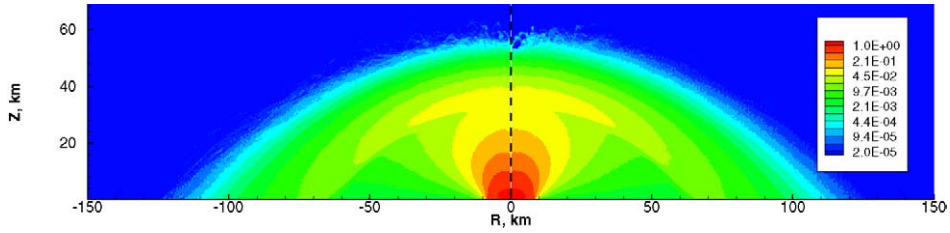

Fig. 2. The number density contours (normalized by the vent number density) of gas plume (left) and virtual SO_2 molecules (right).

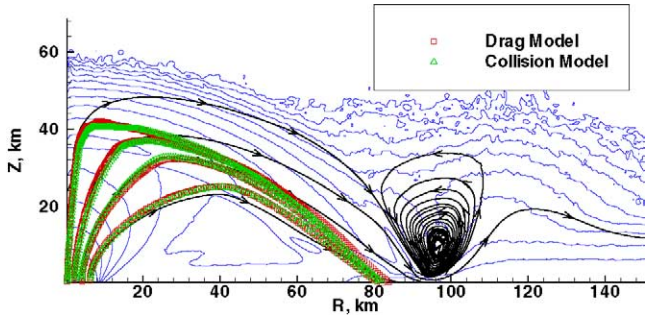

Fig. 3. Comparison of 10 nm particle trajectories calculated with the Collision Model and the Drag Model. Also plotted are the gas number density contours (dotted lines) and the streamlines (solid lines with arrows).

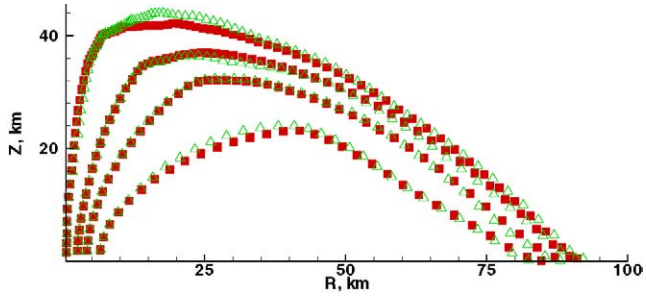

Fig. 4. Comparison of 3 nm particle trajectories calculated with collision weighting factor (△) and without the weighting factor (■).

but N times less frequent, where N is the collision weight. By "N times as effective," it is meant that in each collision the gas molecule is set to be N times more massive. Figure 4 shows the comparison of particle trajectories calculated with and without a collision weighting factor of $N = 5$. The good agreement between the trajectories indicates that the collision weighting method is a reasonable way to reduce computational expense for trajectory calculations of large particles. Note that the small discrepancy between particle trajectories above 40 km in Fig. 4 is caused by the relatively noisy computation of the background gas flow there.

2.4. Column density and shadow calculations

The column density along tangential lines of sight (herein referred to as TCD, i.e., tangential column density) can be calculated by ray tracing. Such calculations are necessary for direct comparison with observations of plume brightness. The angle of the center of the vent source with respect to the limb (ϕ_v) is taken into account in the calculation as shown in Fig. 5a. The plume axis passing through the origin of Io is in the plane of the paper.

The column density at viewing angles other than tangential can be projected onto the surface of Io and interpreted as the shadow cast by the plume if the particle plume that cast the shadow is optically thin. The effects of the plume opacity will be investigated in the future. Figure 5b shows a schematic diagram of this situation. The elongation of the shadow because of the spherical geometry of the surface of Io is also taken into account by allowing the solar ray (line of integration) to intersect with the surface of a sphere of radius of Io and calculating the length of the arc, L_a, as shown in Fig. 5b. Once the line of integration becomes tangential to the surface of Io at the terminator, the plume stops casting a shadow.

3. Results and comparisons

3.1. Parametric study on vent conditions

Two sets of contours (Fig. 6) in vent temperature and velocity (V_v, T_v) space are created from ∼ 40 individual simulations, with one set of contours corresponding to constant shock heights (H_s) and the other to constant ring positions (R_r) at the peak deposition radius, assuming a cold condensing surface. The two sets of contours in vent velocity and temperature (V_v, T_v) space are shown in Figs. 6a and 6b. From these two sets of contours, it is possible to constrain the *unique* vent temperature and velocity for large plumes from an observed shock altitude and deposition ring radius at the intersection of R_r = constant and H_s = constant lines. Since the observed plume height (the maximum height of scatterers in the respective image) of Pele-type plumes ranges from ∼ 300 to 460 km (McEwen et al., 1998), and peak deposition radius from ∼ 500 to 620 km, a reasonable range for this type plume in (V_v, T_v) space is obtained by finding the region enclosed by contours of $R_r = 500$ and 620 km, and $H_s = 260$ and 360 km. This region is indicated in Fig. 6a by the band between two dashed black lines approximately corresponding to contours of $R_r = 500$ and 620 km. Note that our constraints are based on shock heights appropriate for the observed plume heights. For small Prometheus-type plumes, one cannot constrain a *unique* (V_v, T_v) combination from the observed shock height and peak ring radius by this approach, as the two sets of contours in Figs. 6a and 6b

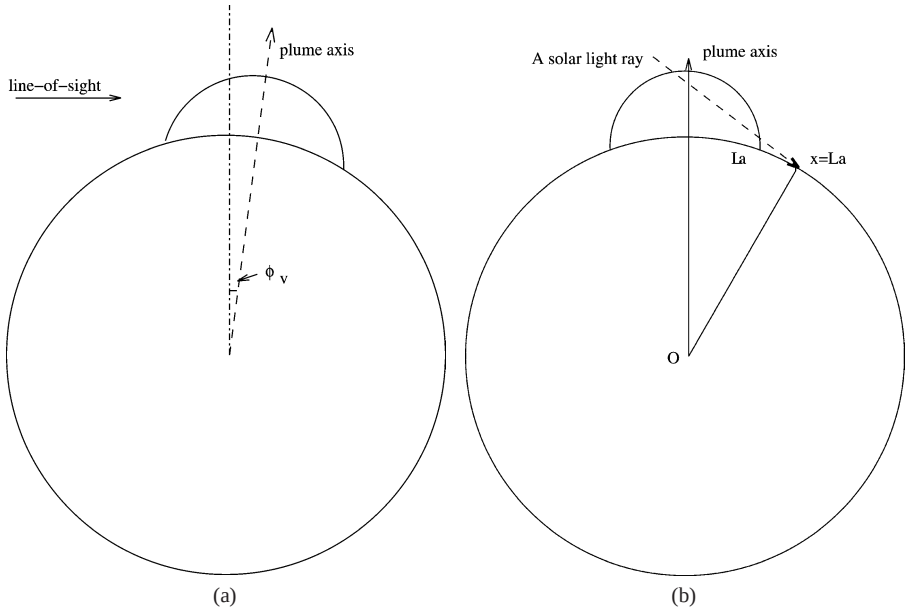

Fig. 5. Schematic of ray tracing calculation of (a) TCD and (b) shadow of plume with the consideration of spherical geometry.

are essentially parallel to each other in the domain of interest. Note that the inability to constrain (V_v, T_v) has nothing to do with the uncertainty in observations. The model predicts that many combinations of (V_v, T_v) would give the same observed shock height and peak ring radius. In the absence of a usable result from the H_s/R_r plots for small plumes, other measures, such as radiation constraints, are necessary to determine the vent conditions more precisely. Despite this, we have attempted to constrain (V_v, T_v) combinations for Prometheus-type plumes as tightly as possible. These ranges are shown on Fig. 6a by a white dashed rectangle. The (T_v, V_v) values in this region produce plumes with shock heights of $\sim$ 35 to 50 km (plume heights of $\sim$ 60 to 80 km) and peak deposition radii of $\sim$ 65 to 105 km. These values are appropriate for Prometheus-type plumes (Strom and Schneider, 1982).

Note that our constrained vent velocity for the Prometheus plume is significantly smaller than the free molecular ballistic estimate of 500 m/s by Strom and Schneider (1982) based on the plume height of $\sim$ 65 km. Because it neglects the gasdynamic shock, the ballistic approximation is clearly inadequate for estimating the vent velocity, and its accuracy is especially poor at high T_v when the high internal energy of the gas and intermolecular collisions contribute appreciably to the development of the plume. The gas flow is accelerated through the conversion of internal energy to kinetic energy during the expansion of the flow. This causes the molecules to rise higher than the ballistic height (for the same mean vent velocity V_v) and to fall further from the vent.

In this parametric study, the number density at the vent, n_v, a third free parameter, has been kept fixed. This is because, as mentioned in Section 2.2, the gas flow fields with different n_v appear to have approximately the same contour shapes: the contour levels are simply scaled by the source number densities. For example, Figs. 7b–7d show the number density contours, normalized by n_v, for three plumes with the same (V_v, T_v) of (200 m/s, 180 K) but different vent number densities ranging from 5×10^{17} to 2×10^{18} m^{-3}. It is seen that the three contours look almost the same. This kind of gas dynamic similarity has been tested for several (V_v, T_v) combinations and is expected to hold for virtually the entire range of the parametric study. However, for this gas dynamic similarity to exist, it is necessary for the flow in the vent vicinity to be in the continuum regime ($Kn < 10^{-4}$ based on vent diameter in our case). For more rarefied vent flows ($Kn \sim 10^{-3}$), the normalized gas density flow field looks different as can be seen by comparing Fig. 7a ($n_v = 5 \times 10^{16}$ m^{-3}) with Figs. 7b–7d. The lower intermolecular collision rate and thus lower radiation losses for lower vent number density plume causes the plume to retain more translational energy and thus to rise higher and expand more widely. We emphasize that a DSMC simulated free-molecular flow is not equivalent to a Stochastic–Ballistic modeled flow. As introduced in the Method section, the molecules generated at the source in DSMC calculations also have random thermal velocities sampled from a Maxwellian distribution at the vent temperature (T_v), and carry equilibrium rotational and discrete vibrational energy.

Because of the virtual independence of plume shape on n_v as long as the near vent flow is near continuum, n_v cannot be constrained by shock height and ring radius observations. An estimate of efflux based on an observed column density or resurfacing rate would be desirable to constrain n_v after the vent diameter and V_v are constrained. For example, an efflux of 1.1×10^{29} SO_2 molecules/s is found to be consistent with such observations at Pele (Zhang et al., 2003a). Hence, if V_v is constrained to be $\sim$ 1000 m/s, then the vent number density is estimated to be around 5×10^{17} SO_2/m^3. A different method to constrain the vent number density is examined in Section 3.2.1.

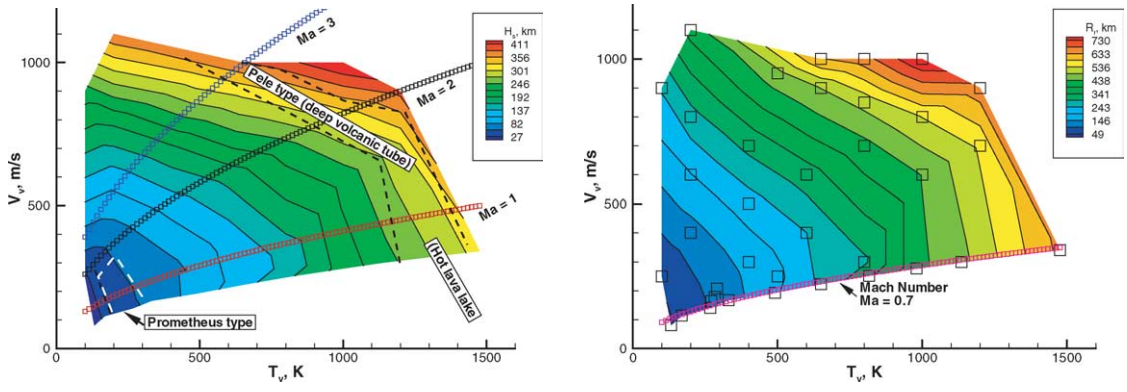

Fig. 6. (a) Constant plume height (H_s) and (b) constant peak frost deposition radius (R_r) contours in vent velocity-temperature (V_v, T_v) space. Suitable regions of (V_v, T_v) for Pele- and Prometheus-type plumes are indicated. Vent conditions corresponding to $Ma = 1$, 2, and 3 are also shown by dotted curves in (a). A lower bounding Ma number of 0.7 relevant to a lava lake plume is shown in (b). The (V_v, T_v) at which the ~ 40 individual simulations were performed are indicated by the square symbols in (b). Note that the (V_v, T_v) domain that will result in a plume larger than a Pele-type plume (upper right) is not covered by the parametric study.

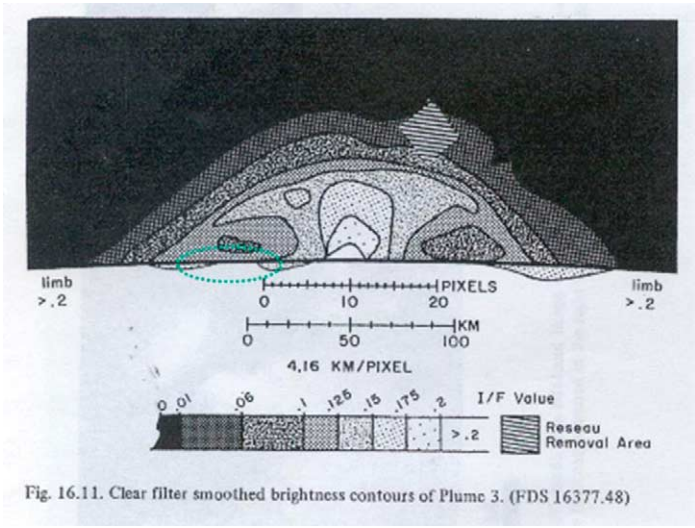

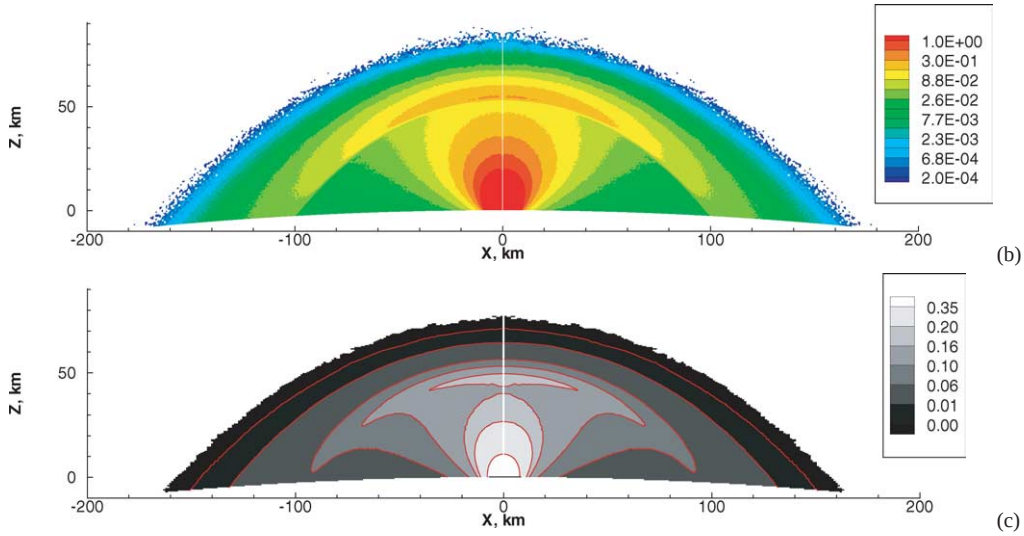

Fig. 8. (a) Voyager image of the brightness of Prometheus plume (*from* Strom, R.G., Schneider, N.M., 1982. Volcanic Eruption Plumes on Io. In: Morrison, D. (Ed.), Satellite of Jupiter. The Arizona Board of Regents. Reprinted by permission of the University of Arizona Press), (b) the number density contours (normalized by 5×10^{16} m^{-3}) of the modeled Prometheus gas plume and (c) the gas TCD (normalized by 6×10^{17} cm^{-2}) for the modeled plume. All three figures are drawn to the same length scale.

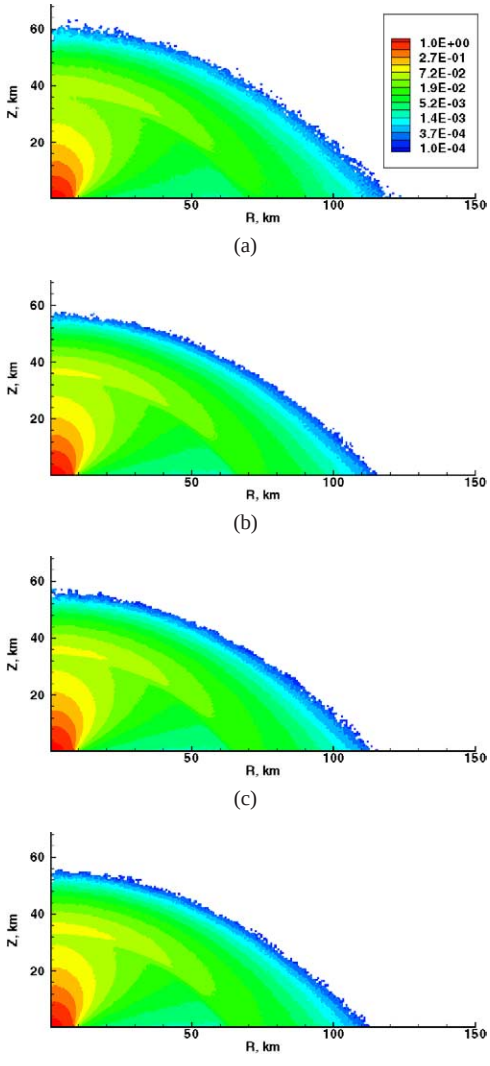

Fig. 7. Number density contours (normalized by the vent number density) of plumes with vent number density of (a) 5×10^{16} m^{-3}, (b) 5×10^{17} m^{-3}, (c) 1×10^{18} m^{-3}, and (d) 2×10^{18} m^{-3}.

3.2. Matching plume, shadow, and deposition ring images

3.2.1. Reproducing Voyager images of the Prometheus plume

Several vent conditions (Fig. 6) were tried and found to produce a good fit to the gas plume shape (height and canopy diameter) for the Prometheus plume observed by Voyager 1 (Strom and Schneider, 1982). The source of Prometheus is 5° in front of the limb of Io during the observation (Strom and Schneider, 1982) in Fig. 8a. A Prometheus-type plume with an evaporating lava lake[4] at 350 K, corresponding to $V_v = 140$ m/s and $T_v = 300$ K, as the source was simulated. The difference in the temperatures of the lava lake and the gas will be explained in Section 4. The resulting plume with this vent condition and a low surrounding frost surface temperature of $T_s = 90$ K is shown in Fig. 8b. It is understood that the Voyager images were taken during ionian day time. A simulated plume image at higher surface temperature will be discussed below. To make a more meaningful comparison to the observation of Strom and Schneider (1982) shown in Fig. 8a, one needs to calculate the plume column density along the line-of-sight, since the brightness of a plume depends on column density of scattering particles. Equation (3) (Collins, 1981) shows the relation between the observed reflectivity and the gas column density for Rayleigh-scattering:

$$Nl = \frac{2N_0^2\lambda^4(I/F)}{\pi^3(n_g^2-1)^2(1+\cos^2\theta)}, \tag{3}$$

where Nl is the observed column density of the gas (in molecules/m^2), N_0 is the gas reference number density (2.68×10^{25} molecules/m^3) at 0 °C and 1013 mbar, λ is the wavelength of the scattered light (m), I/F is π times the measured radiance/solar irradiance at λ, n_g is the index of refraction of the gas (at 0 °C and 1013 mbar, a function of λ), and θ is the phase (scattering) angle. Equation (4) is for Rayleigh-like scattering by very small particles of radius $r < 0.03\lambda$:

$$Nl = \frac{\lambda^4(I/F)}{8\pi^5 r^6(1+\cos^2\theta)}\left(\frac{n_p^2+2}{n_p^2-1}\right)^2, \tag{4}$$

where Nl is the observed particle abundance (in particles/m^2), r is the mean particle radius (m) and n_p is the index of refraction of the particle material. These two equations show that the brightness of a plume is proportional to the column density along the line-of-sight whether the scatterers are gas molecules or small particles. Thus, assuming any entrained particles move with the gas, our gas column density contours could be interpreted as scattered sunlight brightness contours with some proportionality constant. Since we have already obtained the gas density field (in molecules/m^3), the column density along lines-of-sight can be readily calculated via cell-by-cell integration (Fig. 8c). Note that the 5° offset of the source of Prometheus from the limb of Io is taken into account. It is seen that the total gas TCD contours show very encouraging similarities to the Voyager image. In addition to the general shapes and dimensions of the contours, "hatchet" shape TCD contours are seen near the gas shock in both the observation and the simulation.

It is understood that the observed plume brightness probably arises from scattering of sunlight by fine particulates (refractory or volatile) rather than by the gas. In fact, Collins (1981) analyzed the Voyager images of Loki and concluded that the UV brightness of the outer plume cannot be explained by Rayleigh-scattering from the gas but may instead be explained by the Rayleigh-like scattering of very small particles with radii of 1.0–10 nm. Thus, the transport of fine 1–100 nm refractory crystal or droplet-like particles entrained in modeled gas plumes is examined next. It is found that nano-sized particles tend to track the gas flow well. This

[4] See Section 4 for more details.

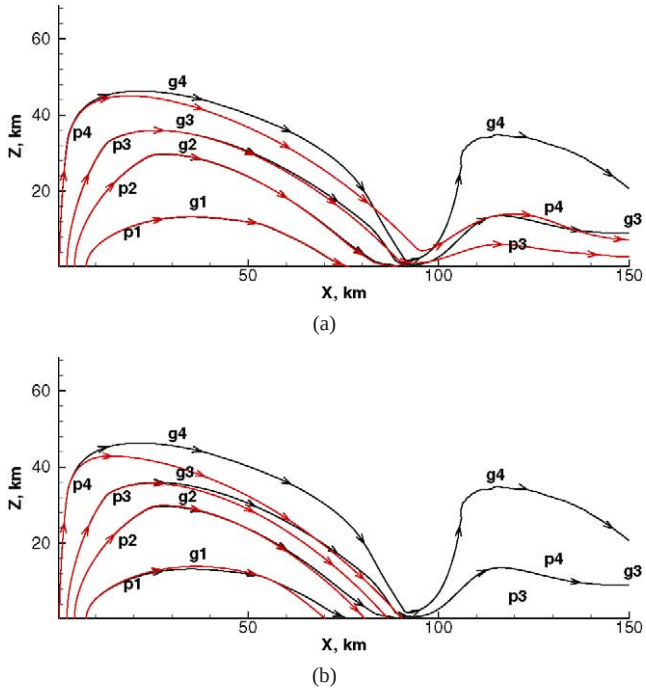

Fig. 9. Comparison of streamlines of gas flow ("g" lines) and that of particles ("p" lines) of different sizes: (a) 1 nm and (b) 3 nm. Notice how some of the smaller particles in (a) bounce with the gas.

tracking is shown in Figs. 9a and 9b which compare the streamlines of the gas and particle flow. The background gas flow in these two figures is the same as that in Fig. 3 with a surface temperature of 110 K and is intended to show the response of these particles to the "bounce" of the gas. It is seen that these particles of size of ~ 1 nm easily track the gas flow and some 1 nm particles from the very outer portion of the canopy also bounce along with the gas although they depart from the gas flow streamlines. That is, the turning flow near the re-entry shock acts like a cyclone separator: the larger particles are sorted from the small ones. Larger particles are less responsive to the accelerating gas flow (cf. Fig. 3).

The flow fields of particles in the modeled nightside Prometheus plume shown in Fig. 8b were then calculated: it was hoped that the TCDs of nano-sized particles would resemble the gas plume TCD and match the Voyager image since nano-sized particles tend to track gas flow well. Figures 10a–10e show the TCD of particles of different sizes. As expected, the TCD images of nano-sized refractory particle plumes indeed show convincing similarities to the Voyager image. Figure 10c shows that the particle TCD differs from the Voyager image for ~ 10 nm particles, especially in the outer portion of the plume (beyond the gas canopy shock): the width and the height of the particle plume decrease and the contours at high altitude coalesce. The differences in the outer portion of the plume between the TCD contours and the Voyager image in Fig. 8a become larger as the particle size is further increased (cf. Figs. 10d and 10e). Thus, Fig. 10 suggests that most of the particles entrained in the *outer* portion of the Prometheus plume are smaller than ~ 10 nm. This is consistent with the photometric analysis of the Voyager image of the similar plume Loki by Collins (1981). He suggested that in the outer portion of Loki, particles are extremely fine with radii of less than ~ 10 nm. Since particles with such small sizes tend to track gas flow well, it is reasonable to use the observed plume shape (height and canopy diameter), visualized by scattering from extremely fine particles, to constrain vent conditions by matching the modeled *gas* flow to the observed particle plume shape. The discussion above does not exclude the existence of larger particles in the vent vicinity. Collins (1981), in fact, suggested that in the reddish inner portion of Loki the ejecta may consist of larger particles (1–1000 μm).

It should be pointed out that the number density of the gas at the vent influences how large the particles can be and still track the gas flow. As shown in Fig. 7, if the source number density of the gas is changed, the gas flow would still have roughly the same contour shapes but the contour levels would scale proportionally. A particle with a radius r would have a certain trajectory, say, trajectory "p2" in Fig. 9, in the gas flow for a particular source number density. If, for a fixed source velocity, the source number density of the gas is increased by some factor N, a particle of size Nr starting at the same point would then have approximately the same trajectory as "p2." This is because, for free-molecular drag, the gasdynamic acceleration of a spherical particle is proportional to n/r, where n is the gas number density. Thus, it is possible that larger particles could track the gas flow if the source gas number density were larger than expected. This feature, in fact, provides another possible constraint on the gas source number density. Since our ~ 10 nm limit is consistent with the Voyager observation of Loki analyzed by Collins (1981), the gas source number density used herein should also be fairly realistic. Future observations of the gas column density at Prometheus would provide additional constraints on the gas source number density.

A relatively high brightness near the surface (the circled region in Fig. 8a) is seen in the Voyager image of Prometheus indicating a slightly higher particle column density there. This feature can also be reproduced by a plume of nano-size particles at a slightly higher surface temperature, as shown on the left-hand side of Fig. 11b illustrating a plume of 1 nm particles entrained in the modeled Prometheus plume (Fig. 11a (left)) with surface temperature $T_s = 108$ K. A "bounce" of a portion of the falling gas from the top of the canopy is seen in Fig. 11a (left). The levitation of 1 nm particles by the bouncing gas and their gradual descent through the subliming atmosphere results in the higher particle column density near the surface. In addition, Fig. 11b shows that the Voyager image of Prometheus is best reproduced by plumes of 1 nm particles entrained in the modeled Prometheus gas plumes with slightly different surface temperatures on the left- and right-hand sides.

The levitation of small particles by the bouncing gas flow is more dramatic around gas plumes over a warmer surface. This is shown in Fig. 12 by the number density contours,

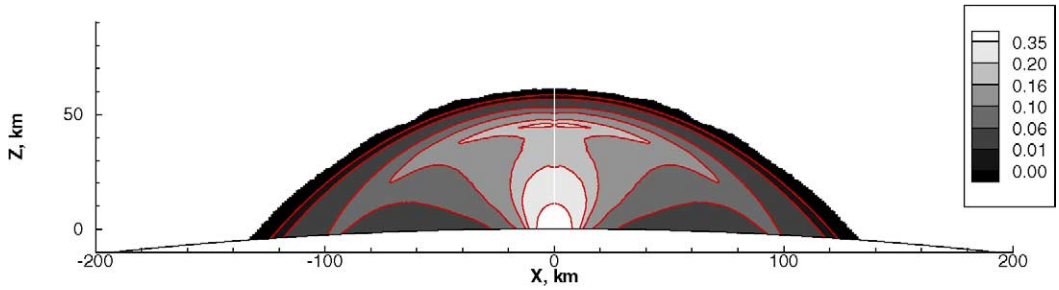

(a)

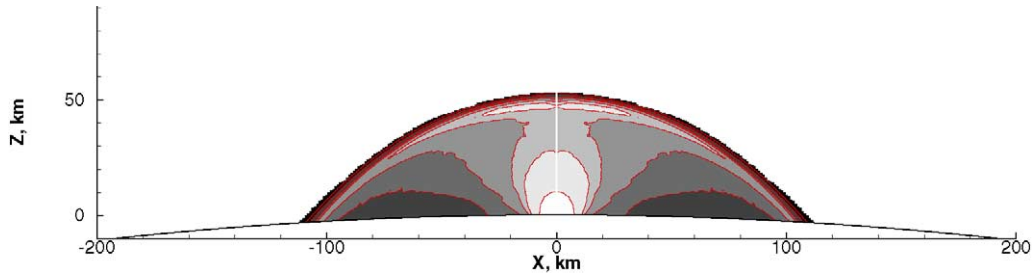

(b)

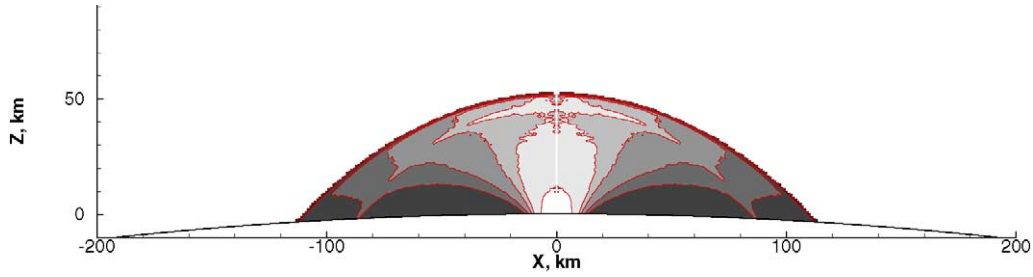

(c)

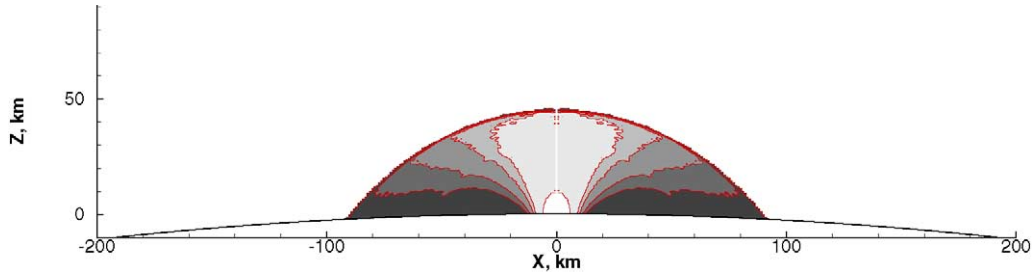

(d)

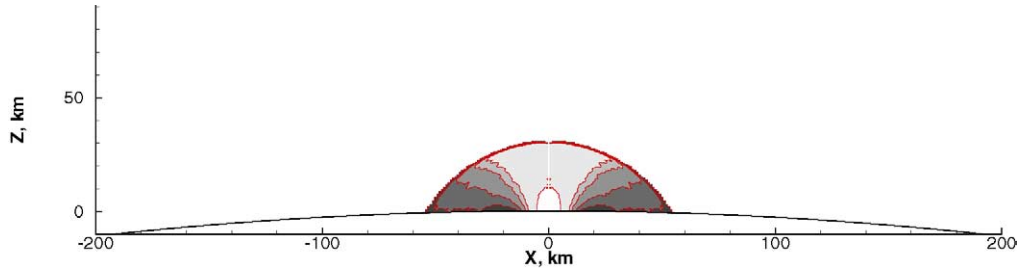

(e)

Fig. 10. The normalized tangential column density (TCD) of (a) 1 nm, (b) 3 nm, (c) 10 nm, (d) 30 nm, and (e) 100 nm refractory particles entrained in the gas plume shown in Fig. 8b. Cases (a) and (b) were calculated by the Collision Model, and the others by the Drag Model.

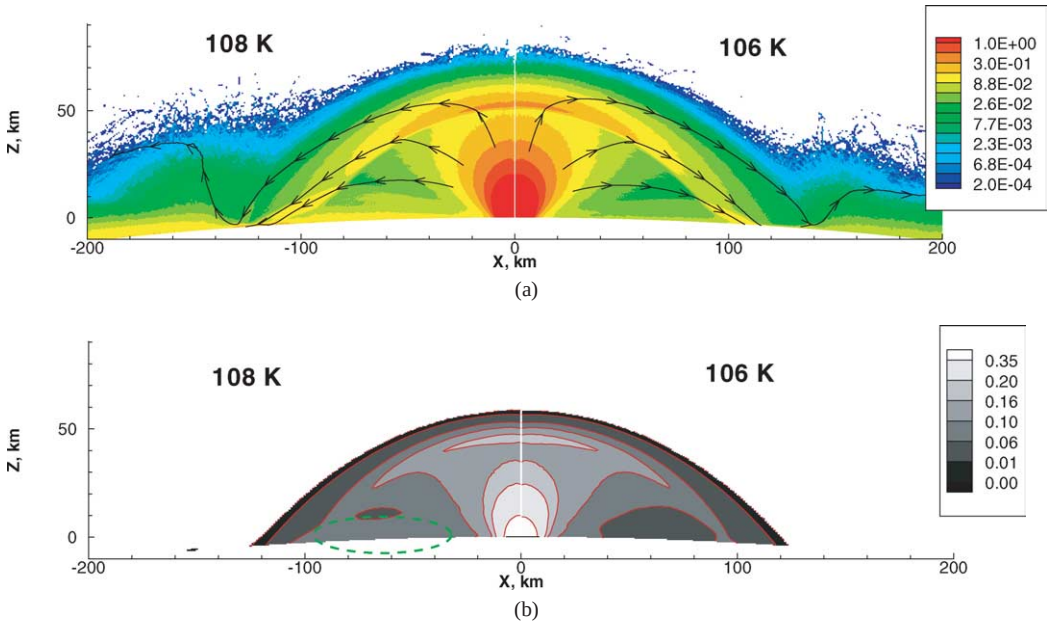

Fig. 11. (a) The number density contours (normalized by 5×10^{16} m^{-3}) of gas plume with surface temperature of 108 K (left) and 106 K (right), (b) the normalized TCD of 1 nm spherical particles entrained in these gas plumes. Note the low altitude circled "dust cloud."

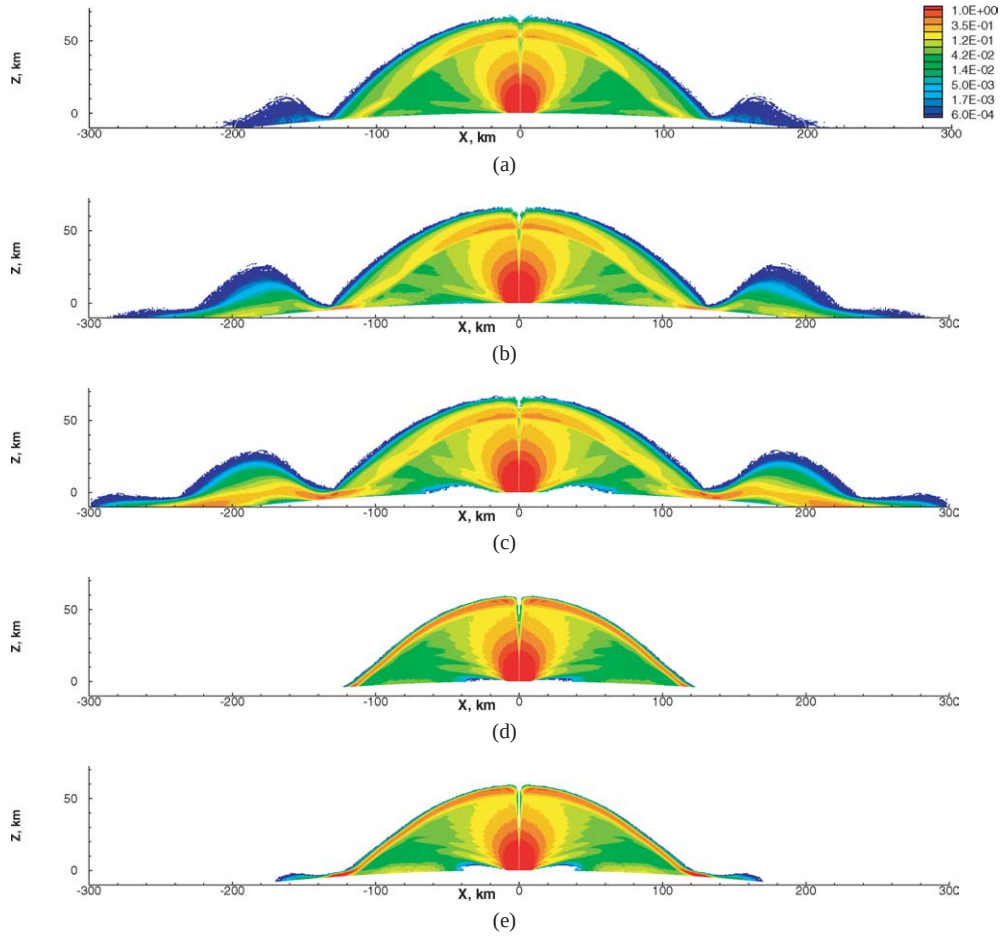

Fig. 12. (a)–(c) The normalized number density (by one tenth of the vent number density) contours of 1 nm dust in Prometheus gas plumes at $T_{surface}$ = (a) 108 K, (b) 110 K, and (c) 112 K; (d) and (e) for 3 nm dust in gas plumes at $T_{surface} = 110$ and 112 K, respectively. There is only a slight bounce of 3 nm particles even at $T_{surface} = 112$ K. Note that the "dimple" along the centerline is caused by insufficient number of dust particles.

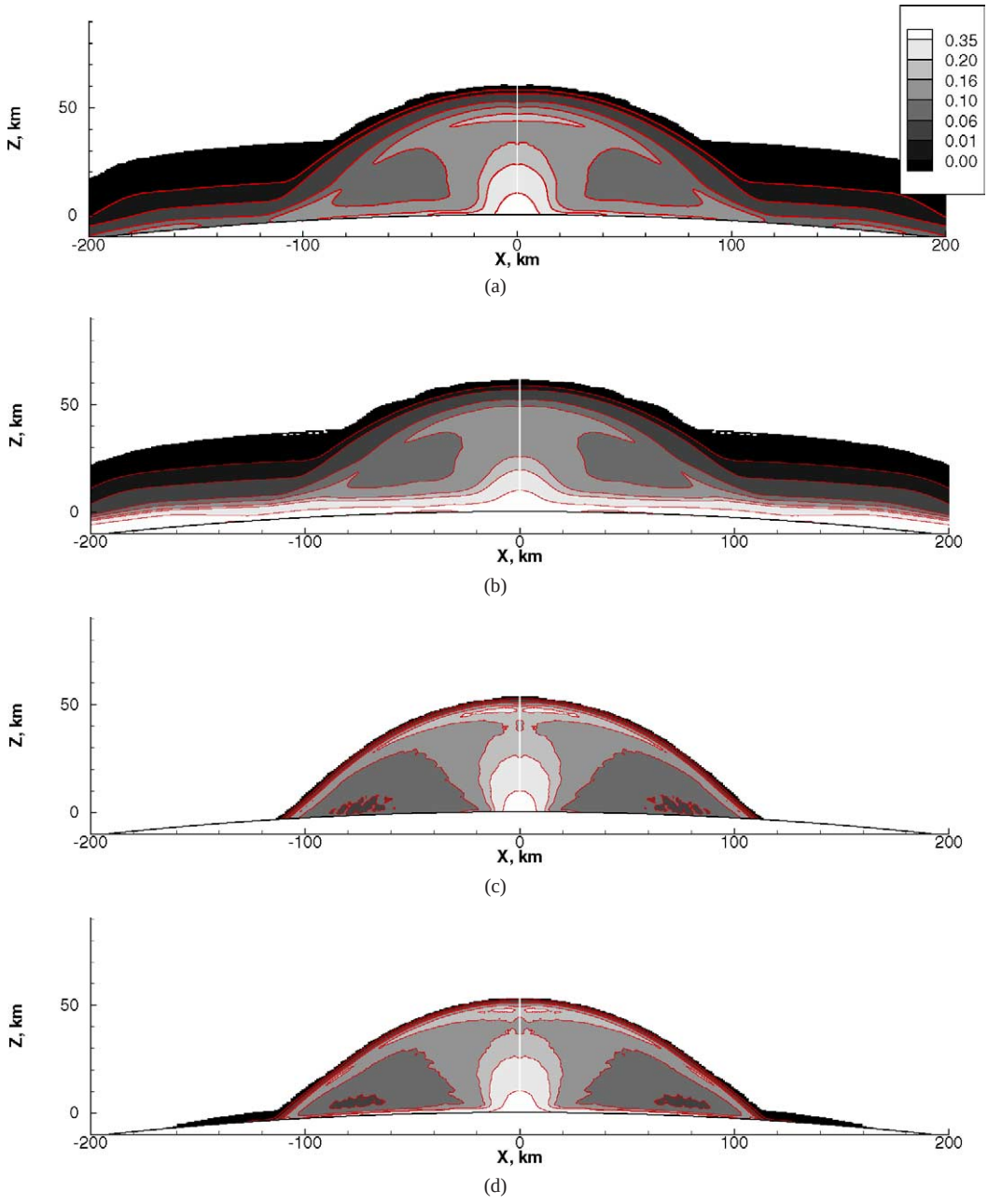

Fig. 13. (a) and (b) The normalized TCD of 1 nm dust at $T_{surface} = 110$ and 112 K, respectively; (c) and (d) 3 nm $T_{surface} =$ at 110 and 112 K, respectively.

normalized by vent number density, of nano-sized particles in Prometheus gas plumes at different surface temperatures. The corresponding TCDs of these plumes are shown in Fig. 13. It is seen that the more dense sublimation atmosphere at high values of $T_{surface}$ supports larger particles, and is responsible for a possible formation of a dust cloud. "Feet" (lateral extensions from the main plume) appear in some of the TCDs either when the surface temperatures are high[5] or the particles are small. There is, in fact, observational evidence suggesting the existence of such "feet" as seen in a Galileo image showing the Pillan plume at almost zero solar zenith angle (Fig. 1.1 in Zhang, 2004). As will be discussed later, the deposition of these suspended particles at large distances from the vent might be the cause of the multiple rings observed around Prometheus (Geissler et al., 2003).

3.3. Settling time and implications of subsolar frost temperature on Io

As suggested above, visible dust clouds might be formed as the result of the "bounce" of small particles along with gas flows. If various plumes are continuously injecting very

[5] We refer to 112 K as a "high" surface temperature because the equilibrium vapor pressure of SO_2 doubles when the surface temperature increases from 110 to 112 K.

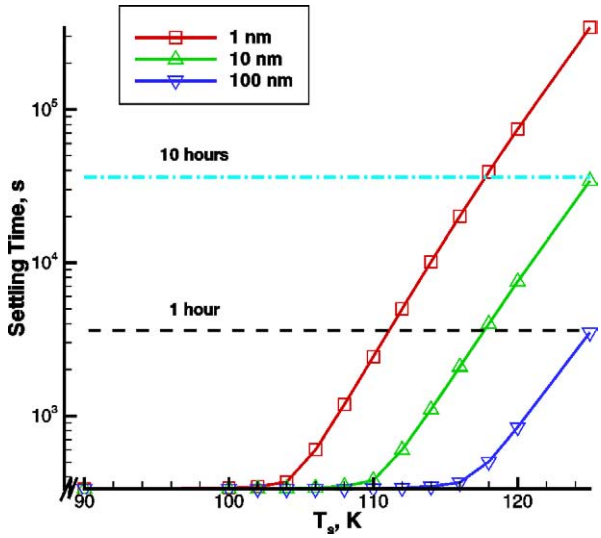

Fig. 14. Settling time of particles of different sizes at different surface temperatures. A one hour settling time is comparable to the flow times associated with a plume while a 10 hour time is comparable to the times surrounding noon when the sunlit surface is warmest.

small particles into the region well above any sublimation atmosphere, one could anticipate the formation of thin dust clouds as particles gradually fall to the surface. We next examine why no such clouds have been reported.

The falling time of particles with different sizes starting at rest at 100 km above[6] the surface in an isothermal, hydrostatic, sublimation atmosphere is here defined as the settling time and determined numerically for different surface temperatures. The particle equation of motion is:

$$-mg + \frac{1}{2}C_d \rho u^2 \sigma = m\frac{du}{dt}, \tag{5}$$

where m is the mass of a particles, g is gravitational acceleration on Io (1.8 m/s^2), C_d is the free-molecular drag coefficient (Eq. (2)), $\rho = \rho_0 e^{-z/L}$ is the local mass density of the atmosphere and ρ_0 is calculated based on the equilibrium vapor pressure at the surface temperature T, u is the vertical velocity of the particle, $L = RT/g$ is the scale height of the isothermal sublimation atmosphere and σ is the cross-sectional area of particle. Note that the free-molecular drag has a u^2 dependence which is different from the u dependence of the drag in continuum regime. Figure 14 is a semi-log plot illustrating the results of this calculation. The settling times are plotted in the figure as a function of surface temperature for particles of different sizes. As expected, the smaller the particle or the higher the surface temperature, the longer the settling time. At very low surface temperatures, particles fall almost ballistically in ~ 200 s since the sublimation atmosphere is very tenuous. At high surface temperatures, the settling time increases approximately exponentially with surface temperature. The exponential dependence starts at lower surface temperature for smaller particles. The location of settling time equal to ten hours (corresponding to about a quarter of an ionian day) is indicated in Fig. 14 by a dash-dotted line. The intersection of this line with the settling time profiles for potentially observable particles provides some constraints for subsolar frost temperature. If the particles in the "bounce" are observable, the absence of a more distant dust cloud on Io implies that the settling time of particles is small compared to the duration of ionian day. Since the "feet" that appear in some of the TCD contours shown in Fig. 13 have comparable brightness to the plume itself, the particle cloud should be observable if the plume is. Therefore, the absence of dust clouds on Io seems to indicate that the subsolar surface temperature is relatively low. For example, if a cloud of 1 nm particles is potentially observable, the intersection of the ten hour line and settling time line for 1 nm particles in Fig. 14 shows that the subsolar frost temperature is lower than ~ 118 K.

Our assumptions about particle temperature and the nature of gas–particle collisions affects the value of the free-molecular drag coefficient C_d. In the above calculations, it is assumed that particles are cold and the gas–particle collisions are specular. Different assumptions lead to somewhat different drag coefficients. Fortunately, the constraints on subsolar surface temperature suggested by Fig. 14 based on different assumptions for drag coefficient do not vary by more $\sim 1\%$.

3.3.1. *Reproducing Voyager images of the Pele plume*

Strom and Schneider (1982) showed that a Voyager image of Pele had remarkable features that distinguished Pele from other plumes known then. First, Pele is huge with a plume height of ~ 300 km and canopy diameter of ~ 1200 km. A bright top appears in the smoothed ultraviolet images of Pele. Strom and Schneider suggested that this top is caused by a concentration of particles at a shock front. By following the particle trajectories we have shown that refractory particles finer than ~ 10 nm, dragged by the gas flow, could reach the shock and concentrate there (Zhang et al., 2003b). Here we compute the particle number density and then the TCD of the particles for comparison with the Voyager image. First, since our gas TCD of Prometheus appears to be very similar to the Voyager image of this plume (Fig. 8a), the same calculation was done for the Pele plume and similarities between the calculation and observation were sought. Figure 15 shows such a comparison. Note that the 10° distance of Pele center behind the limb when the Pele image was taken by Voyager is taken into account in all the TCD calculations in this section. One sees that the calculated gas TCD contours are indeed qualitatively quite similar to the brightness contours in the Voyager image, especially near the shock. Such a distinct shock feature does not appear in the Voyager image of Prometheus (cf. Fig. 8b). The relatively small variation in number density near the shock in Prometheus hides the existence of a gas shock in the TCD.

[6] Note that particles fall virtually ballistically above one scale height (~ 10 km) for about 200 s which is small compared to the settling times considered (hours) so the starting height is not significant.

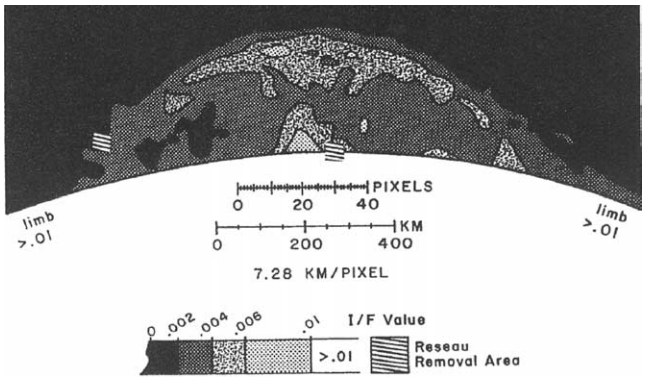

(a)

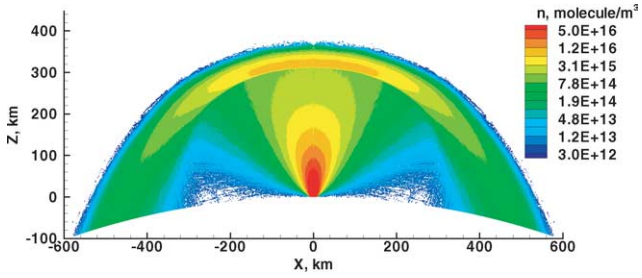

(b)

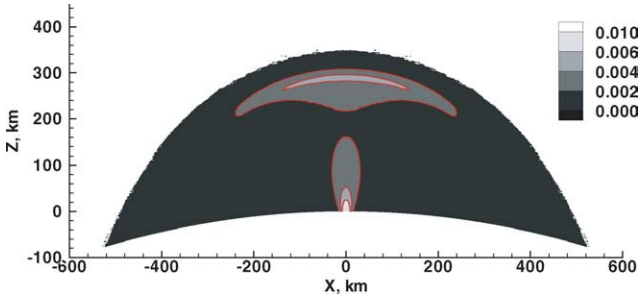

(c)

Fig. 15. (a) Voyager image of the ultra-violet brightness of Pele (*from* Strom, R.G., Schneider, N.M., 1982. Volcanic Eruption Plumes on Io. In: Morrison, D. (Ed.), Satellite of Jupiter. The Arizona Board of Regents. Reprinted by permission of the University of Arizona Press), (b) the number density contours of the modeled Pele gas plume and (c) the gas TCD (normalized by 4.5×10^{19} cm^{-2}) for the modeled plume. The observed plume and the simulated plume are drawn to the same length scale. Note the calculated TCD below the limb is blanked.

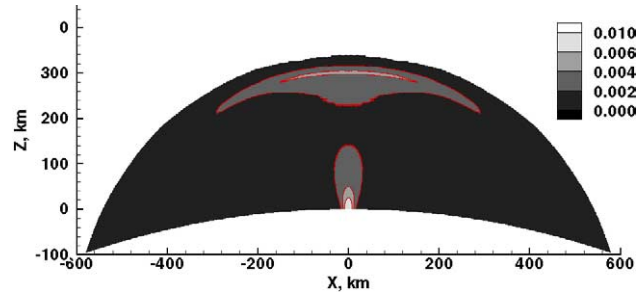

(a)

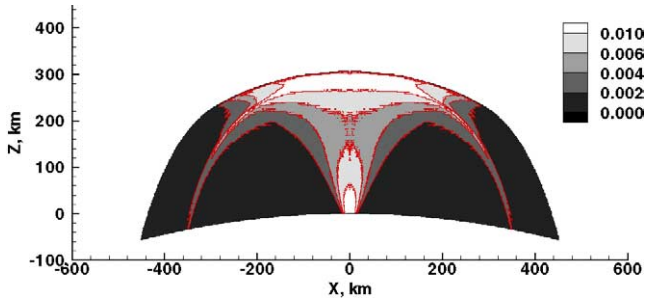

(b)

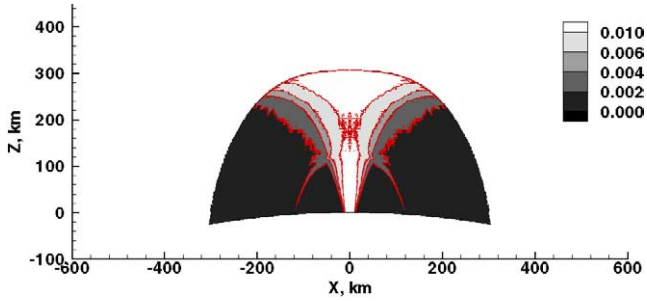

(c)

Fig. 16. The normalized tangential column density (TCD) of (a) 1 nm, (b) 10 nm, (c) 100 nm refractory particles entrained in the plume shown in Fig. 15b except for plume (a) where the gas plume was the early nominal Pele-type plume with the flat surface and constant g approximations, and the plume was deformed into spherical geometry. The scales have been adjusted in each figure to enhance the details of the structures (the normalized TCDs at the vent are 0.015, 0.1 and 0.03 for (a), (b), and (c), respectively). Notice the double-shock-like feature in (b) and (c). Further details can be found in Zhang et al. (2003b).

We observe that the simulated TCD of $\sim 2 \times 10^{17}$ cm^{-2} near Pele's shock is consistent with the SO_2 gas column abundance of $\sim 3.7 \times 10^{17}$ cm^{-2} obtained by Spencer et al. (1997) based on an HST observation but assuming a uniform hemispherical gas plume.

The TCDs for entrained fine refractory particles are shown in Fig. 16. As for the Prometheus simulations, it is found that the particles entrained in the Pele plume can be at most about 10 nm in size if they are to follow the gas flow for the nominal source gas number density chosen. This is especially true in the outer portion of the plume. Figure 16a shows that the TCD contours for 1 nm particles are very similar to that of the gas (Fig. 15c). Unlike the particle flow in Prometheus discussed in Section 3.2.1, particles as large as 100 nm in Pele can still reach and rise above the gas shock at ~ 310 km altitude, so the particle size range in the outer portion (beyond the gas shock) of Pele may be wider than that of Prometheus.[7] This wider particle size range is consistent with the particle size estimates of less than 0.08 μm in Pele by Spencer et al. (1997), instead of 0.01 μm in Loki suggested by Collins (1981). However, as seen in Figs. 16a–16c, only particle of sizes on the order of 1 nm reproduce the observed brightness contour shape well especially near the canopy shock. According to Eq. (4), 1 nm particles are far less effective in scattering sunlight than 10–100 nm par-

[7] However, the large particles cannot track the gas flow in the outer portion of Pele and they show a different signature near the gas shock as seen in Fig. 16c.

ticles. Therefore, the flow near the shock must be dominated by ~ 1 nm particles. Using Eq. (4) and assuming the value of $n_p = 1.9$ of Spencer et al. (1997), the column density of 1 nm particle needs to be $\sim 1 \times 10^{19}$ cm^{-2} in order to produce an I/F value of 0.004 at 0.35 μm wavelength. This particle column density is two orders of magnitude higher than the gas column density. This is apparently quite unrealistic. However, due to the r^6 dependence of the light scattering efficiency, far fewer particles that are only slightly larger are needed to produce the observed I/F value, and these particles still track the gas flow quite well. For example, three orders of magnitude lower particle column density is needed for 3 nm particles, and 1.6×10^4 times lower column density is needed for 5 nm particles in order to produce the observed I/F value. It is also understood that large particles could reach high altitude if they are created by condensation in the plume. In fact, large fluffy snow-flake-like particles track the gas flow much better than do spherical particles. This better response to the gas for snow-flake-like particles is observed in our simulations.

It must again be pointed out that the discussion above does not exclude the existence of larger micron-size particles, especially in the vent vicinity. In fact, the brightness in the vent vicinity of Pele observed by Voyager is likely due to large particles of various sizes. The cone shape contours in the vent vicinity in the Voyager image of Pele are different from the "finger" shape contours shown in Fig. 16. This cone shape might be the signature of large-particle flow. Figure 17a shows an example TCD computed for a particle cloud with a log-normal size distribution, and with the r^6 dependence of particle scattering efficiency indicated in Eq. (4). The contour shape is quite similar to that in the vent vicinity in the Voyager image of Pele (cf. Fig. 15a). A better match to the Voyager image can also be obtained by overlaying Fig. 17a on Fig. 16a to simulate an image representing the injection of two classes of particles at the vent; tiny ~ 1 nm grains or droplets perhaps forming from a condensate and larger 5–10 μm dust having a log-normal size distribution. Note that a size distribution seems to be necessary since we observed in our simulations that a plume of particles of a single size cannot reproduce the contour shapes.

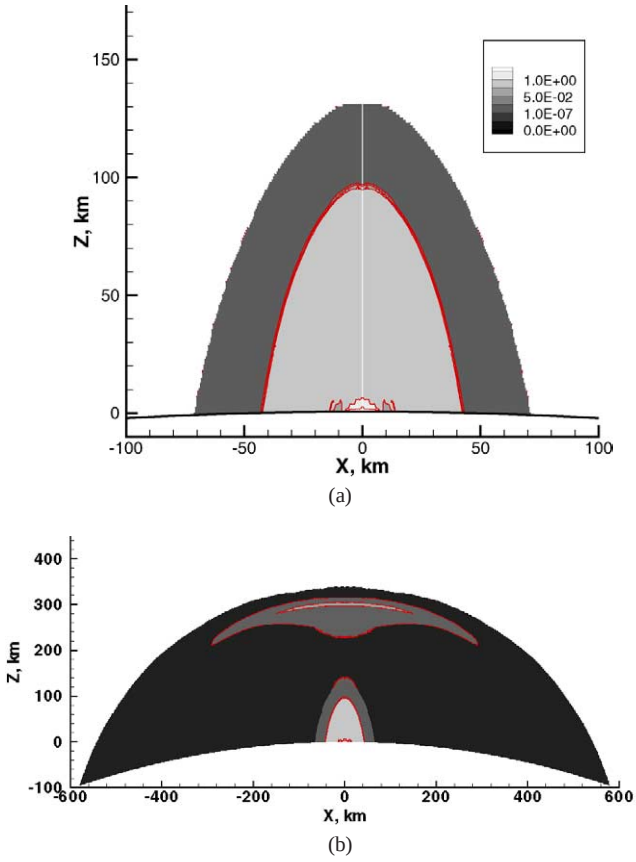

Fig. 17. (a) TCD contours of particles with size ranging from 5–10 μm with a resolution of 0.25 μm. The particle size distribution is log-normal with $n_{5\ \mu m}/n_{10\ \mu m} = 100$. The gas plume is a nominal Pele plume shown Fig. 15b. (b) A better match to the Voyager image is obtained by faked overlaying of figure (a) on Fig. 16a without the consideration of the population relation between 1 nm particles and the large micron-size particles.

3.4. Reproducing plume shadows observed by Galileo

A remarkable reddish shadow cast by Prometheus is seen in the Galileo image shown in Fig. 18a. Several features appear in the image of the shadow: two components seem to be present with one corresponding to a dark "finger" and another to a "mushroom"; there is an asymmetry about the "finger" from north to south with the northern part of the shadow a little weaker and appearing to have a gradient in color while the southern part is relatively uniformly dark. An effort was made to reproduce these features by computing the shadows of particle plumes with particles having different sizes. The solar zenith angle at the Prometheus vent was $\sim 76.4°$ when the image in Fig. 18a was taken. The normalized column densities (without consideration of opacity) projected from the sun onto Io's surface at this angle were calculated for the particle plumes shown in Fig. 10 and plotted in Figs. 18b and 18c. The "finger" shape discussed above is found to be best reproduced by a plume of ~ 30 nm particles. The uniformly dark southern "mushroom" shape may be reproduced by ~ 80 nm or smaller particles. It should be pointed out that it is also possible that there are two distinct dust jets and a non-axisymmetric vent flow (Douté et al., 2002).

Similar calculations were conducted for the Pele gas plume, and the results are shown in Fig. 19. Perhaps someday a Pele shadow may be observed. Because of the large size of the Pele plume, only the lower part of the plume casts a shadow on the surface at high solar zenith angles ($\gtrsim 50°$).

3.5. Gas and particle deposition patterns for Pele- and Prometheus-type plumes

3.5.1. Gas deposition patterns

Our previous results showed that the deposition pattern of the Pele plume varies as the temperature of the surrounding

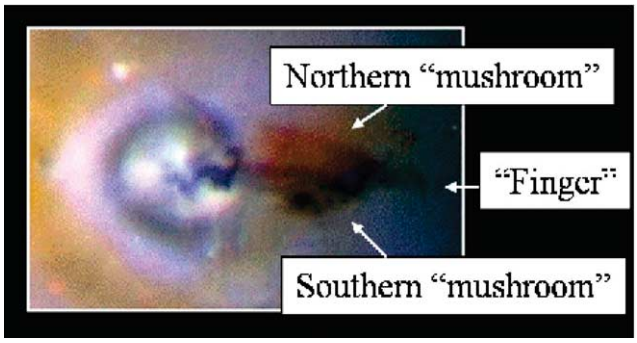

(a)

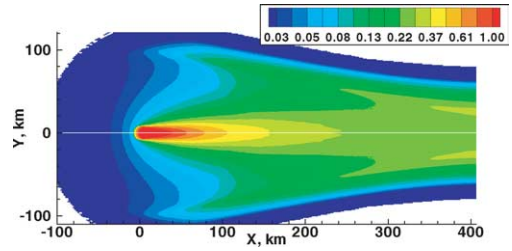

(b)

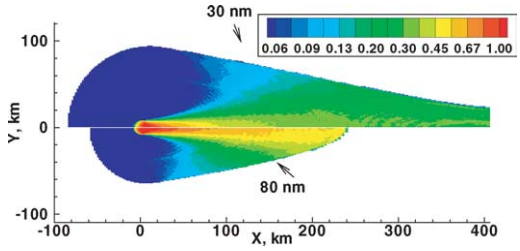

(c)

Fig. 18. (a) Galileo image (http://photojournal.jpl.nasa.gov/catalog/PIA00703) of close-up views of Prometheus; (b) Computed shadow cast on the surface by 1 nm particles; Shadow of 30 nm (top part of (c)) and 80 nm particles (bottom part of (c)). The simulated shadows and the inset of Prometheus in Galileo image are drawn to the same length scale.

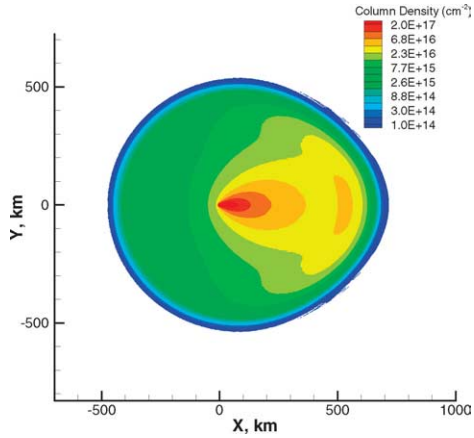

(a)

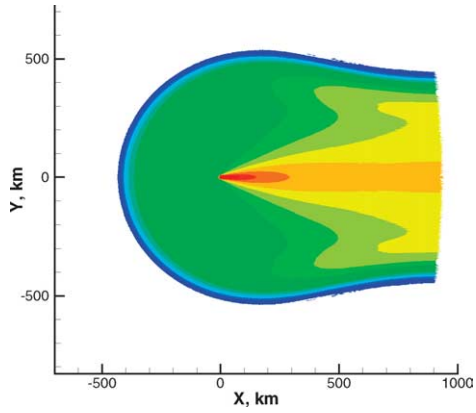

(b)

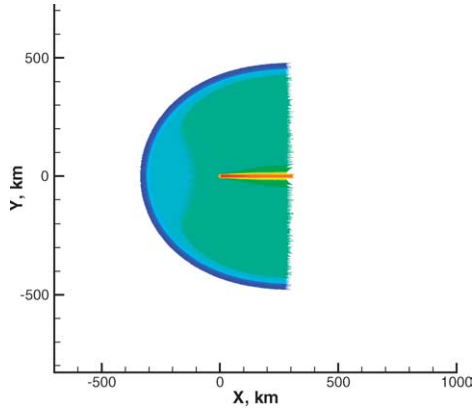

(c)

Fig. 19. Shadow of gas in Pele plume at three different solar zenith angles: (a) 40°, (b) 60°, and (c) 80°. The contour levels are arbitrary and are only chosen to illustrate the general shape of different shadow patterns. The origin is located at Pele's vent.

frost-covered surface changes during the ionian day (Zhang et al., 2003a). At low surface temperatures, the falling gas simply pours onto the surface and condensation dominates to build up a deposition peak. As the surface temperature increases and the sublimation atmosphere thickens, the SO_2 frost begins to be eroded away below the turning point of the impinging flow. We have made similar calculations for Prometheus and the results are shown in Fig. 20. Note that the simulated plumes used here are the ones with vent condition identical to that of the plume shown in Fig. 8b. The effect of erosion by the plume during the day when surface temperatures are high is seen for Prometheus as it was for Pele. Because the deposition profile also varies with time, one needs to calculate the time-averaged deposition profile to make a meaningful comparison with the observed multiple ring structure (Geissler et al., 2003) and examine the possibility of forming such rings by gas deposition. To do so, the deposition profiles for several different surface temperatures were weighted by the duration of time during the day the surface experienced that temperature and averaged over an ionian day. The surface temperature as a function of time of ionian day is based on the work of Kerton et al. (1996) (their Fig. 3). Since Prometheus is a small plume having little variation in latitude, the deposition around it is assumed to be symmetric around the vent. Figure 21 shows such a diurnally-averaged deposition profile. It is seen that the averaged profiles have approximately the same peak deposition

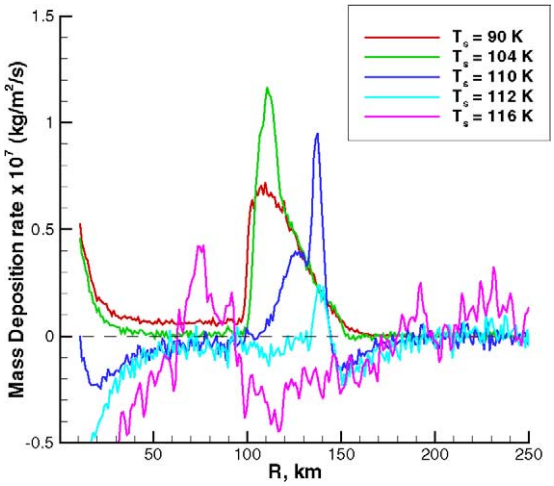

Fig. 20. Deposition profiles around the Prometheus plume as a function of distance from the vent at different surface temperatures. Note that the profiles are blanked near the vent for $R < 10$ km.

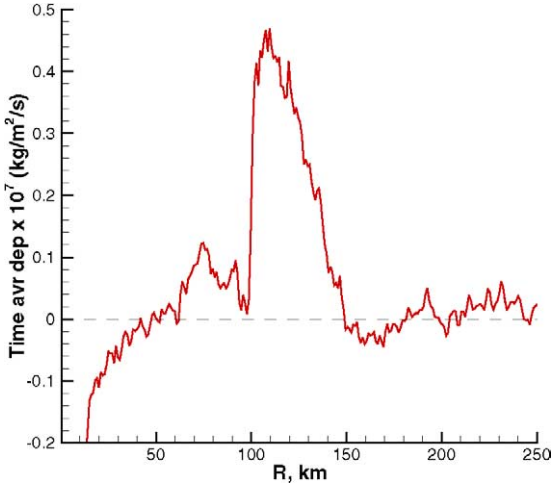

Fig. 21. Diurnally averaged gas deposition profiles with peak subsolar temperature T_{ss} of 116 K for Prometheus.

radius (110 km) as the nightside plume ($T_s = 90$ K curve in Fig. 20). Hence, the use of the nightside deposition profile to represent the peak deposition radius in the parametric study of vent conditions in Section 3.1 is justified. It is seen in Fig. 21 that there is a strong ring at $R = 100$–150 km and indications of a couple of possible other rings at radii inside and outside R of 150 km.

Another interesting feature of the deposition ring is its sharp inner edge when the surface temperature is low. This is a reflection of the extension of the canopy shock all the way to the surface. The abrupt change in the gas density across the shock near the intersection of the shock and the surface causes the jump in the flux to the surface.

3.5.2. Particle deposition patterns

We have shown that there is a sorting mechanism for particles inside the gas plume: the motion of large particles tends to decouple from that of the gas, and thus large particles generally rise less and land closer to the vent than do smaller ones Zhang et al. (2003b). This sorting mechanism exists in Prometheus. Figures 22a–22b illustrate the normalized deposition profiles of relatively large refractory particles. Note the distinct edges of the particle rings compared to the gas condensation ring. The figure suggests that multiple rings might be the result of the deposition of different size particles at different distances from the vent. Unlike the deposition of the gas frost and nano-size particles, the deposition profiles of larger particles (> 10 nm) are very weak functions of the surface temperature. Figures 22a and 22b compare the deposition of particles in a nightside and dayside Prometheus plume. The precipitation of these particles near the turning region of the gas flow over a warmer surface results in this insensitivity. One should note the especially narrow deposition ring for 10 nm particles compared to gas or to larger particles.

The deposition profiles of nano-particles in plumes with relatively high surface temperatures are shown on a log scale in Fig. 22c. Outer rings are indeed seen in these profiles. Thus, we suggest that the outer rings (at $R > 110$ km) around Prometheus discussed by Geissler et al. (2003) are likely caused by the deposition of small nano-size particles that followed the gas through its "bounce" (Fig. 9a) below the re-entry shock. Bigger particles simply would not be carried through the "bounce" by the low density gas flow (Fig. 3).

The deposition profiles of different size particles in a nightside Pele plume are plotted in Fig. 23. An interesting feature is that the particles tend to deposit in distinct bands with a sharp rise in deposition at the band inner edge. These particle bands occur at different locations than the gas deposition ring. Quite coincidentally, the narrow deposition ring discussed for Prometheus for 10 nm particles also appears for particles of this size in Pele-type plumes. Figure 23 shows that the deposition band for 10 nm particles is quite narrow compared to the bands for large particles and frost (gas condensation). This may be caused by the similar dynamic pressure of the gas inside both Pele and Prometheus plumes (similar density and velocity at the vent and near the shock) although there are appreciable differences in the plume sizes. Similar dynamic pressure of the gas results in similar drag on the particles.

4. Discussion

4.1. Physical significance of modeled vent parameters

The dependence of Pele's vent pressure on vent temperature has been calculated by Zolotov and Fegley (2001) based on the HST observed SO_2/S_2 and SO_2/SO ratios in the plume (McGrath et al., 2000; Spencer et al., 2000). However, the vent appropriate for the model of Zolotov and Fegley (2001) and our model should be distinguished. The vent temperatures they assumed are high (around 1700 K) in agreement with the recent Galileo NIMS observations by

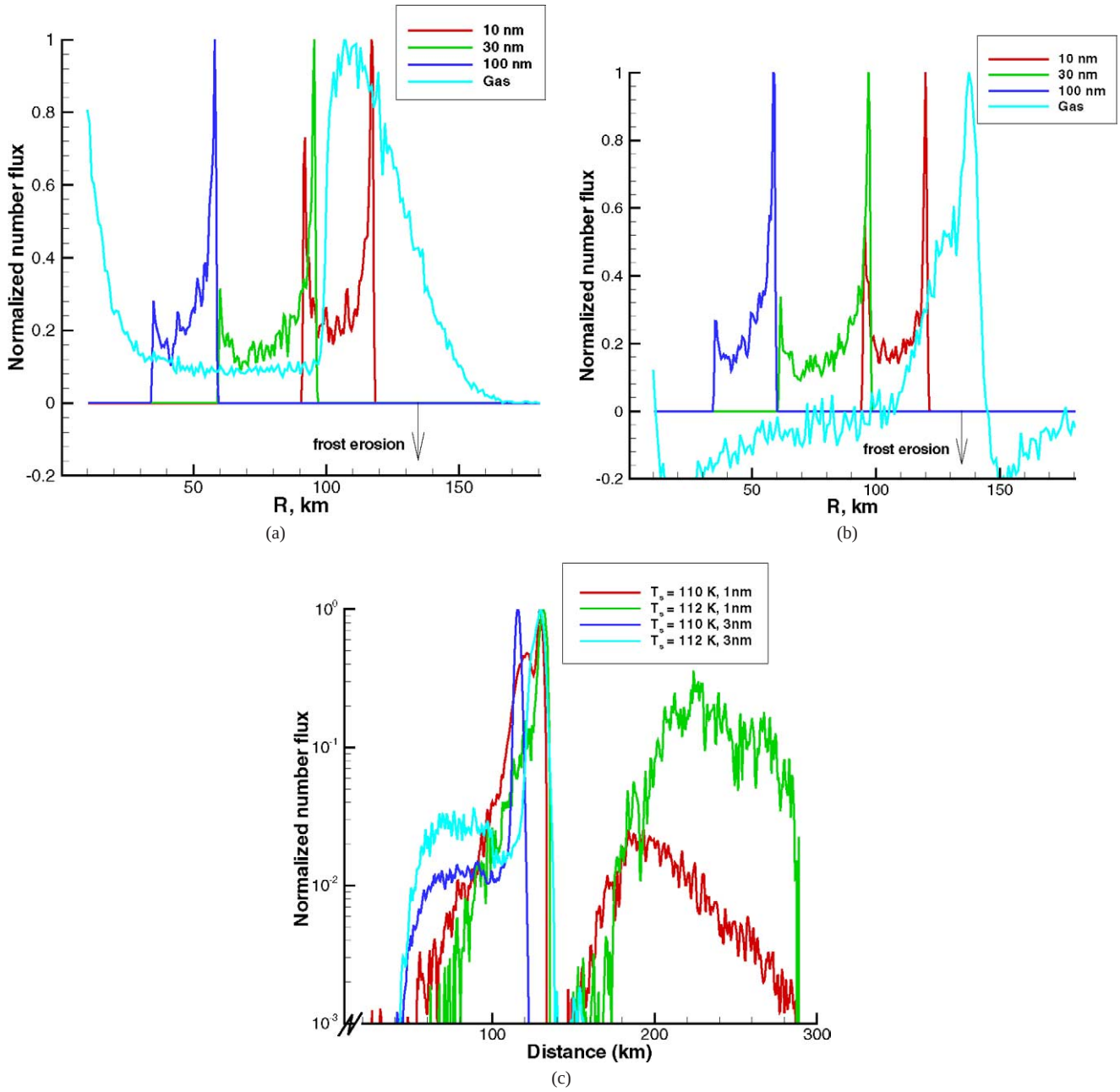

Fig. 22. Deposition profiles (normalized by peak rate) of different size refractory particles entrained in (a) a night side ($T_s = 90$ K) Prometheus plume and (b) a day side ($T_s = 110$ K) plume, and also deposition of the gas. (c) Deposition profiles of small particles in plumes with relatively high surface temperatures plotted on a log scale to illustrate the small net deposition at large radius from the vent. Note the possible explanation of the outer deposition ring by this profile.

Lopes-Gautier et al. (2002). Zolotov and Fegley (2001) calculated a total vent pressure, for the observed gas species, of 0.01–2 bar in this temperature range (∼ 1700–2000 K). However, this result is drastically different from our previous vent conditions—we found a vent static pressure of only ∼ 40 nbar ($p_v = n_v k T_v$) and best fit temperature of 650 K for Pele.

There thus remains the question of what our modeled vent really represents. Degassing from a lava lake or intrusions of lava into surface SO_2 frost accumulations appear to be more realistic source mechanisms for Prometheus than venting from a deep round tube (Kieffer et al., 2000). We propose that our modeled vent should be interpreted as a "virtual" vent representing the location—a relatively "clean" plane—where the gas temperature and velocity reach the modeled values. A schematic diagram of such an virtual vent is shown in Figs. 24a and 24b for a volcanic tube and lava lake plume, respectively. Our virtual vent is not necessarily right at the exit of a volcanic tube or at the same location appropriate to the model of Zolotov and Fegley (2001). Our virtual vent is assumed to be close to the exit where the flow has expanded and the temperature has dropped below the lava

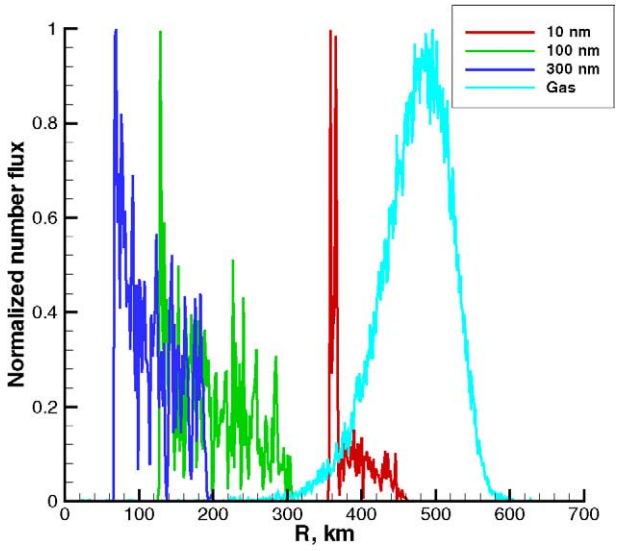

Fig. 23. Normalized (by peak rate) deposition profiles of refractory particles of different sizes entrained in a night side Pele plume. Also shown is the gas deposition profile for comparison.

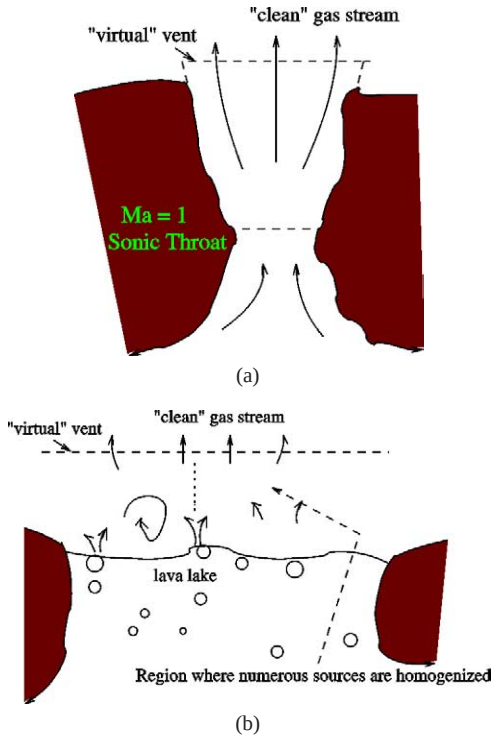

Fig. 24. Schematic diagram of "virtual" vent.

temperature. A modeled vent diameter of ∼ 16 km in this context is thus reasonable. The match to the Voyager image of Prometheus we obtained provides further support of this idea. The contour dimension in the vent vicinity is on the order of 10–20 km in the Voyager image. A likely scenario for the source of Prometheus is that a large number of bubbling sites of dimension of ∼ 10–100 m are distributed over a region of ∼ 20 km in size. We have recently modeled this kind of volcanic plume with a diffusing disk (simulating an evaporating lava lake) as the source. We do so by specifying a temperature and a reasonable number flux at the disk with the same size as our nominal vent (∼ 8 km in radius). A bounding steady-state Mach number of ∼ 0.7 adjacent to the disk is found regardless of the disk temperature. Further details are discussed in the next subsection. For the Pele plume seen in the Voyager image (cf. Fig. 15a), the contour dimension in the vent vicinity is even larger and on the order of 100 km though the image saturation in the vent vicinity may also contribute to the large size of the contours. This case may be similar to Prometheus except that the bubbling sites are replaced by deeper cracks or holes. Our calculations show that a diffusing disk at ∼ 1700 K could also be a possible source for Pele. Interestingly, this is consistent with the high lava temperature observed at Pele (Lopes-Gautier et al., 2002), and this is the reason we mark a hot "lava lake" region in Fig. 6a for Pele.

The "virtual" vent idea appears to be a little arbitrary. This situation is caused by the relatively large uncertainties involved in observation. If there were an "exit"—the "clean" plane parallel to the surface as shown in Figs. 24a and 24b—where every relevant parameter, such as the width of the gas stream crossing the plane, the gas temperature and velocity, could be simultaneously determined by observation, then we believe that our model would reproduce the plume flow well. Unfortunately, this is not the case for the observations on Io. We know almost nothing definite at the vent, nor has a vent been observed directly. Thus, it should be very useful if, in the future, an attempt was made to measure the gas velocity, and temperature and spatial extant of the gas stream at a well defined location, say a certain plane parallel to the surface. It is understood that this is a difficult task for remote sensing.

Given the current situation, what can we say more specifically about our modeled vent and the vent conditions constrained by the model? First, the "virtual" vent must be close to the actual exit. For example, as mentioned earlier in this section, a diffusing disk at ∼ 1700 K could also be a possible source for a Pele-type plume. In that simulation, the flow reaches Mach 3 (from Mach ∼ 0.7 at the disk) within ∼ 15 km above the disk. This is a relatively short distance compared to the height of a Pele-type plume.

Second, the most important parameters at the vent are the velocity (V_v) and temperature (T_v) because they determine the kinetic and internal energy of the gas and ultimately the height and width of the plume. Other parameters—the vent size, the number density at the vent, the vibrational degrees of freedom and vibrational relaxation numbers, opacity of the gas and the presence of other species—appear to perturb the plume height and width slightly, usually about 10–20% (Zhang, 2004). Thus, the constraints on the vent conditions (T_v, V_v) obtained in the present work are felt to be reasonably accurate.

In the lava lake plume simulations, the gas pressure in the hot lava lake vicinity is still in the range of tens to hundreds

of nbar which is much less than the equilibrium SO_2 vapor pressure over lava at a high lava temperature. It should be noted that equilibrium is not reached when there is a steady-state dynamic expansion with the vapor generated at the surface expanding into a near vacuum. Therefore, the dynamic expansion must be considered when linking the calculation of vent pressure by Zolotov and Fegley (2001) to the resulting escaping gases. Note that we assume the chemistry of the volcanic gases is quenched at the "virtual" vent in our simulation.

It should be pointed out that the dynamic expansion from the lava vicinity to our "virtual" vent is presumably very complex due to radiative heating of the gas from the hot lava, gas radiative losses to space, and possible mixing of the gas from different degassing spots (say, from along a fissure in the crust of a lava lake). In fact, Douté et al. (2002) suggested that the ejection of gas at Prometheus lava front cannot be axisymetric. A detailed investigation, beyond the scope of the present work, is needed to examine the process that connects the degassing in the lava and the virtual vent region.

4.2. Kinetic theory analysis of steady-state Mach number associated with the evaporating gas into a vacuum

In our lava lake plume simulations, there appears to be a steady-state, lower bounding Mach number of ~ 0.7 right above the diffusing lava for all lava temperatures as shown in Figs. 6a and 6b. To find out why this is the case, one needs to find the distribution function (f_1) for the molecules between a diffusing surface and a vacuum boundary at steady-state. The distribution function (f_0) of the velocity component (u_z) normal to the diffusing surface for the diffusively generated molecules (source molecules) is,

$$f_0 = 2\beta^2 u_z e^{-\beta^2 u_z{}^2}, \tag{6}$$

where $\beta = \sqrt{m/(2kT)}$ is the reciprocal of the most probable molecular thermal speed. Note that the source molecules are not the same as the ones between the diffusing surface and the vacuum boundary (or in the first cell adjacent to the diffusing surface) at steady-state. The molecules in the first cell are, in fact, the slower moving ones that are left behind; faster molecules escape the first cell preferentially. The population of molecules of class u_z left in the first cell after a sufficiently long time interval of Δt is,

$$\frac{l}{u_z \Delta t} f_0 \, du_z, \tag{7}$$

where l is the length of the first cell in the direction normal to the surface. The distribution function (f_1) for these molecules is thus proportional to f_0/u_z which returns back to a half-Maxwellian ($u_z > 0$ only) distribution after normalization:

$$f_1 = \beta/\sqrt{\pi} e^{-\beta^2 u_z{}^2}. \tag{8}$$

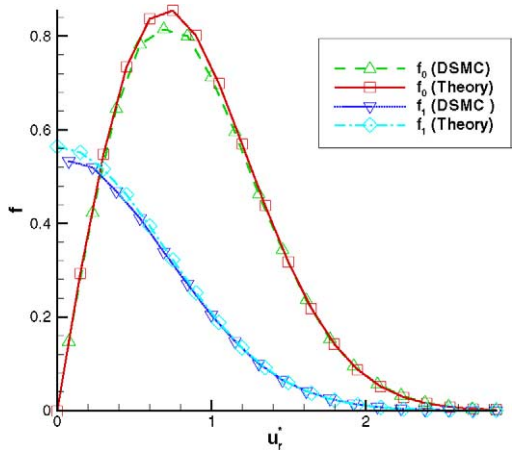

Fig. 25. Distribution function, both from theory and sampled in DSMC, of $u_z^* = \beta u_z$ for diffusively generated molecules (f_0) and the molecules between a surface and a vacuum boundary at steady-state (f_1). Note the half-Maxwellian distribution for the flowing molecules between the surface and the vacuum.

Therefore, the mean z velocity of the molecules flowing between the diffusing surface and the vacuum boundary is,

$$\bar{u}_z = \int_0^\infty u_z f_1 \, du_z \left(\int_0^\infty f_1 \, du_z \right)^{-1} = \frac{1}{(\sqrt{\pi}\beta)}, \tag{9}$$

which gives a Mach number right around 0.7 for SO_2. Note that since the velocity distribution f_1 is not strictly Maxwellian, the "temperature" of the gas averaged over all the molecules in the first cell is not the same as the diffusing disk temperature T_0. This is why there is a difference between the lava temperature and the gas temperature in our simulated lava lake Prometheus plume discussed in Section 3.2.1.

The above analysis is validated by the DSMC calculation. Figure 25 shows that the velocity distribution for the molecules adjacent to the diffusing surface is essentially the half-Maxwellian just as expected.

4.3. Source of the extremely fine particulates in the outer portion of Prometheus

The small particles in the outer portion of the Prometheus plume discussed in Section 3.2.1 could be dust or pyroclastic particles entrained in the gas plume, or volatile SO_2 snow-flakes, droplets and/or crystals that form via condensation in the plume. Both refractory particles and volatile condensates may be present. Although none of these possibilities can be excluded yet, the plausibility of particles formed via condensation in the plume is examined briefly. In fact, the conditions in the plume away from the vent vicinity are quite favorable for these particles to form through intermolecular collisions. Figure 26 shows the contours of the ratio of the local gas pressure (nkT, where n is the local gas number density, k is the Boltzmann constant, and T is the local gas temperature) to the local equilibrium vapor pres-

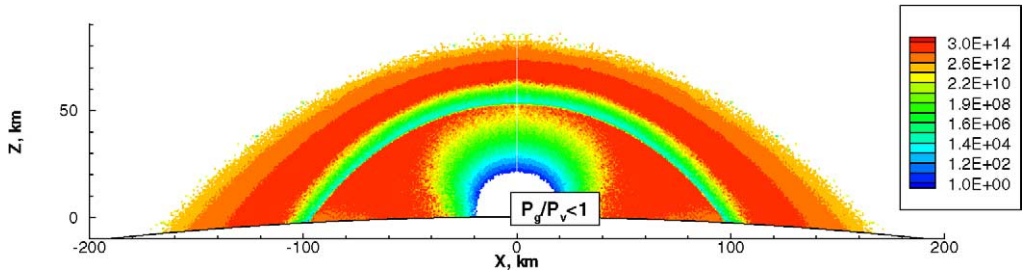

Fig. 26. The ratio of local gas pressure to the equilibrium vapor pressure for a simulated Prometheus-type gas plume same as that in Fig. 8b. Notice the logarithm color bar. The regions in the vent vicinity where the ratio is less than one are blanked. Colors indicate possible condensation.

sure (Ingersoll et al., 1985) ($P_{\text{vapor}} = 1.52 \times 10^{13} e^{-4510/T}$) for a Prometheus-type plume. The figure indicates that most regions within the Prometheus plume away from the vent vicinity are highly super-saturated, and the conditions are favorable for condensation. It is not yet certain if collision rates are sufficient to grow substantial particles or whether the temperature of such particles is even close to the local gas temperature. It is also understood that P_{vapor} is that over a macroscopic sheet of ice and the nano-particles may have a different equilibrium vapor pressure. Moreover, the kinetic temperature in non-equilibrium conditions that occur in many locations of the plume may be misleading. Still, it is likely that as the gas plume cools via both expansion and radiation, some condensation occurs inside the plume. The particles formed (SO_2 snow-flakes, droplets and/or crystals) may be very fine (< 10 nm) and track the gas flow in the outer portion of the gas plume accounting for the Voyager observed plume brightness in those regions. In fact, Kieffer (1982) had a detailed discussion of condensing vapor for both an equilibrium and a non-equilibrium situation, and suggested that condensation of SO_2 could occur in an expanding flow and the condensate particles would be generally less than 100 nm. It has also been shown that, for a sticking coefficient of 0.1, the maximum size of particles that could grow through condensation of SO_2 is ~ 50 nm (Moore et al., 2003).

We are presently adapting the computational code to model the condensation/evaporation of droplets.

4.4. Subsolar frost temperature on Io—implication of relative significance of volcanic/sublimation atmospheres

Our modeling suggests that the observed lateral extension of the Pillan plume (cf. the "feet" discussed in Section 3.2.1) and multiple ring structure around Prometheus imply that the temperature of frost near the subsolar point is greater than ~ 110 K. Combining this with the upper limit we suggested in Section 3.3, the subsolar frost temperature range would be ~ 110–118 K. It is interesting that the corresponding density of a SO_2 sublimation atmosphere for subsolar frost temperatures in this range is precisely in the range to play a significant role in the gas dynamic interactions with plumes, the parameters of which are independently chosen. Rathbun et al. (2003) obtained a subsolar surface temperature of ~ 133 K based on the Galileo photopolarimeter–radiometer (PPR) observation. However, though this was not pointed out by Rathbun et al. (2003), a careful examination of the surface temperature map (their Fig. 1) near the subsolar point reveals that high subsolar surface temperatures seem to be correlated with dry surfaces (dark area) with little frost coverage while relatively low surface temperatures (less than 120 K) are observed in bright areas presumably covered with frost. Therefore, our constraint on the subsolar frost temperature appears consistent with the Galileo PPR observation.

Ingersoll (1989) pointed out that "the key unknowns for Io are the strength of the volcanic sources and the temperature of frost near the subsolar point." The recent Galileo PPR observation (Rathbun et al., 2003) gives a better understanding of subsolar surface temperature. However, the relative significance of volcanic/sublimation atmosphere is still controversial. Our modeling suggests constraints on these unknowns, i.e., a subsolar frost temperature of 110–118 K, virtual vent velocity of ~ 150 m/s for Prometheus-type plumes and ~ 900 m/s for Pele-type plumes and a source number density at the virtual vent of $\sim 5 \times 10^{17}$ molecules/m^3 for both types of plumes, with an virtual vent diameter of ~ 16 km. Thus, the relative significance of volcanoes or frost in maintaining the atmosphere on Io may be assessed. On the nightside, the surface temperature is low so that the only substantial atmospheres are beneath the plumes and the length scale associated with each plume can be obtained from Fig. 6. In plumes the vertical column density drops quite rapidly with distance from the vent. The column density decreases by an order of magnitude within 100 km for both type of plumes (Zhang et al., 2003a). The only place where a sublimation atmosphere will play an important role is on the dayside around the subsolar region because of the rapid variation of vapor pressure with temperature. The column is dominated by the volcanic plume within $R \cong 100$ km, while the sublimation atmosphere plays an important role farther away from the vent, where the plume is only a small perturbation (Zhang et al., 2003a). However, the relative significance of plume atmosphere is discussed above in terms of column density. The relative role may not be the same for other observations like inferred temperature or species composition of the atmosphere. We have shown that although the column density is dominated by

the sublimation atmosphere ∼ 100 km away from the vent, the plume locally rises way above and blankets the sublimation atmosphere (Zhang et al., 2003a). The plume gas shows dramatic dynamic features such as a canopy and re-entry shocks and bounces. Therefore, even when both sublimation atmosphere and volcanic plumes are present at the same time, and the sublimation atmosphere dominates the value of the column density, volcanic plumes may still play important roles in other aspects of the atmosphere like its temperature, interaction with the plasma and radiation from space and its composition. Thus, when discussing the relative significance of volcanic/sublimation atmosphere, one must be specific about the particular aspect one is interested in. For example, the effect of the Prometheus plume on the atmospheric temperature inferred by Jessup et al. (2003) should be assessed. Similarly, the effect of plumes on the interaction of the upper atmosphere with the plasma torus and radiation from space should be studied; Wong and Johnson (1996) neglected volcanic plume flows in their model.

5. Conclusions

A parametric study of vent conditions has been performed with certain assumptions about the vent region of ionian volcanic plumes, notably the source gas number density and the vent size. A "virtual vent" was defined for our gas dynamic model applicable to either volcanic or lava lake plumes. With such a definition, a virtual vent of 1–10 km in diameter appears reasonable. Two sets of iso-contours in vent temperature and velocity (T_v, V_v) space were created; one set corresponded to constant shock heights and the other to constant deposition ring positions. Effective vent condition ranges appropriate to both Pele- and Prometheus-type plumes are obtained by matching the shock height and the observed peak deposition ring radius of the visible images. A unique determination of vent conditions is possible for a Pele-type plume.

The dilute flow of refractory nano-particles entrained in the gas plumes was modeled with two "overlay" techniques. The column densities along tangential lines-of-sight were calculated and compared with Voyager plume images near the limb. Encouraging matches with Voyager observations were obtained for both the gas and nano-particle TCDs in both Pele- and Prometheus-type plumes. The calculated TCD of gas near the shock is consistent with that inferred from HST observation (Spencer et al., 1997). An upper limit on the size of spherical particles that can track the gas flow in the outer portion of the plume was found to be ∼ 10 nm. We believe that some of these particles are likely formed through condensation in the gas plume although further study of this issue is required. The shadows cast by Prometheus' particle plumes are computed and compared to a Galileo image. Multiple particle sizes best explain the observed image but nano-particles must dominate. The multiple ring deposition around Prometheus is more likely to be explained by deposition of nano-particles than by (diurnally-averaged) gas deposition. The particles that are ejected from the volcanic source are levitated by the gas "bounce" as they fall toward the warm surface so that they are deposited further from the source. The absence of any observed more distant dust clouds suggests that the subsolar frost temperature is less than ∼ 118 K, assuming that a cloud of 1 nm particles would be observable.

Acknowledgments

The work at the University of Texas at Austin was supported by the NASA Planetary Atmospheres Program, Grant No. NASA NAG5-8143 and an NASA STScI archive grant. We also thank K. Retherford, P. Geissler, R. Lopes-Gautier, M. Zolotov, S. Keiffer, R. Strom, and the anonymous referee for their helpful comments and suggestions.

References

Austin, J.V., Goldstein, D.B., 1995. Direct numerical simulation of low-density atmospheric flow on Io. In: Capitelli, M. (Ed.), Molecular Physics and Hypersonic Flows. Kluwer Academic, Dordrecht, pp. 749–758.

Austin, J.V., Goldstein, D.B., 2000. Rarefied gas model of Io's sublimation driven atmosphere. Icarus 148, 370–383.

Bird, G.A., 1994. Molecular Gas Dynamics and the Direct Simulation of Gas Flows. Oxford Univ. Press, London.

Collins, S.A., 1981. Spatial color variations in the volcanic plume at Loki, on Io. J. Geophys. Res. 86, 8621–8626.

Douté, S., Lopes, R., Kamp, L.W., Carlson, R., Schmitt, B., the Galileo NIMS Team, 2002. Dynamics and evolution of SO_2 gas condensation around Prometheus-like volcanic plumes on Io as seen by the near infrared mapping spectrometer. Icarus 158, 460–482.

Geissler, P.E., McEwen, A.S., Phillips, C., Keszthelyi, L., Spencer, J., 2003. Surface changes on Io during the Galileo mission. Proc. Lunar Planet. Sci. Conf. 34. Abstract 1596.

Ingersoll, A.P., 1989. Io meteorology: how atmospheric pressure is controlled locally by volcanos and surface frosts. Icarus 81, 298–313.

Ingersoll, A.P., Summers, M.E., Schlipf, S.G., 1985. Supersonic meteorology of Io: sublimation-driven flow of SO_2. Icarus 64, 375–390.

Jessup, K., Spencer, J., Ballester, G., Howell, R., Roesler, F., Vigel, M., Yelle, R., 2003. The atmospheric signature of Io's Prometheus plume and anti-jovian hemisphere: evidence for a sublimation atmosphere. Icarus 169, 197–215.

Kerton, C.R., Fanale, F.P., Salvail, J.R., 1996. The state of SO_2 on Io's surface. J. Geophys. Res. 101, 7555–7564.

Kieffer, S.W., 1982. Dynamics and thermodynamics of volcanic eruptions: implications for the plumes of Io. In: Morrison, D. (Ed.), Satellites of Jupiter. Univ. of Arizona Press, Tucson, pp. 647–723.

Kieffer, S.W., Lopes-Gautier, R., McEwen, A., Smythe, W., Keszthelyi, L., Carlson, R., 2000. Prometheus: Io's wandering plume. Science 288, 1204–1208.

Lellouch, E., 1996. Io's atmosphere: not yet understood. Icarus 124, 1–21.

Lellouch, E., Paubert, G., Moses, J.I., Schneider, N.M., Strobel, D.F., 2003. Volcanically emitted sodium chloride as a source for Io's neutral clouds and plasma torus. Nature 421, 45–47.

Lopes-Gautier, R.M.C., Kamp, L.W., Douté, S., Smythe, W.D., Carlson, R.W., McEwen, A.S., Geissler, P.E., Kieffer, S.W., Leader, F.E., Davies, A.G., Barbinis, E., Mehlman, R., Segura, M., Shirley, J., Soderblom, L.A., 2002. Io in the near infrared: near-infrared mapping spectrometer

(NIMS) results from the Galileo flybys in 1999 and 2000. J. Geophys. Res. 106, 33053–33078.

McEwen, A.S., Keszthelyi, L., Geissler, P., Simonelli, D.P., Carr, M.H., Johnson, T.V., Klaasen, K.P., Breneman, H.H., Jones, T.J., Kaufman, J.M., Magee, K.P., Senske, D.A., Belton, M.J.S., Schubert, G., 1998. Active volcanism on Io as seen by Galileo SSI. Icarus 135, 181–219.

McGrath, M.A., Belton, M.J.S., Spencer, J.R., Sartoretti, P., 2000. Spatially resolved spectroscopy of Io's Pele plume and SO_2 atmosphere. Icarus 146, 476–493.

Moore, C., Zhang, J., Goldstein, D.B., Varghese, P.L., Trafton, L.M., 2003. Modeling of particulates and condensates in Io's Pele-type volcanic plumes. Proc. Lunar Planet. Sci. Conf. 34. Abstract 2102.

Moses, J.I., Zolotov, M.Y., Fegley, J.B., 2002. Photochemistry of a volcanically driven atmosphere on Io: sulfur and oxygen species from a Pele-type eruption. Icarus 156, 76–106.

Rathbun, J.A., Spencer, J.R., Tamppari, L.K., Martin, T.Z., Barnard, L., Travis, L.D., 2003. Mapping of Io's thermal radiation by the Galileo photopolarimeter–radiometer (PPR) instrument. Icarus 169, 127–139.

Sartoretti, P., Belton, M.J.S., McGrath, M.A., 1996. SO_2 distributions on Io. Icarus 122, 273–287.

Spencer, J.R., Jessup, K.L., McGrath, M.A., Ballester, G.E., Yelle, R., 2000. Discovery of gaseous S_2 in Io's Pele plume. Science 288, 1208–1210.

Spencer, J.R., Sartoretti, P., Ballester, G.E., McEwen, A.S., Clarke, J.T., McGrath, M.A., 1997. Pele plume (Io): observations with the Hubble Space Telescope. Geophys. Res. Lett. 24, 2471.

Strobel, D.F., Wolven, B.C., 2001. The atmosphere of Io: abundances and sources of sulfur dioxide and atomic hydrogen. Astrophys. Space Sci. 277, 271–287.

Strom, R.G., Schneider, N.M., 1982. Volcanic eruption plumes on Io. In: Morrison, D. (Ed.), Satellites of Jupiter. Univ. of Arizona Press, Tucson, pp. 598–633.

Wong, M.C., Johnson, R.E., 1996. A three-dimensional azimuthally symmetric model atmosphere for Io, 1. Photochemistry and the accumulation of a nightside atmosphere. J. Geophys. Res. 101, 23243–23254.

Zhang, J., 2004. Simulation of gas dynamics, radiation, and particulates in volcanic plumes on Io. PhD dissertation.

Zhang, J., Goldstein, D.B., Gimelshein, N.E., Gimelshein, S.F., Levin, D.A., Varghese, P.L., 2001. Modeling low density sulfur dioxide jets: application to volcanoes on Jupiter's moon Io. AIAA paper 2001–2767 presented at 35th AIAA Thermophysics Conference, Anaheim, CA, June 11–14, 2001.

Zhang, J., Goldstein, D.B., Varghese, P.L., Gimelshein, N.E., Gimelshein, S.F., Levin, D.A., 2003a. Simulation of gas dynamics and radiation in volcanic plumes on Io. Icarus 163, 182–197.

Zhang, J., Goldstein, D.B., Varghese, P.L., Gimelshein, N.E., Gimelshein, S.F., Levin, D.A., Trafton, L.M., 2003b. DSMC modeling of gasdynamics, radiation and fine particulates in ionian volcanic jets. In: Ketsdever, A., Muntz, E.P. (Eds.), Proceedings of 23rd International Symposium on Rarefied Gas Dynamics. AIP Conf. Proc., vol. 663. AIP, New York, pp. 704–711.

Zhang, J., Miki, K., Goldstein, D.B., Varghese, P.L., Trafton, L.M., 2003c. Modeling of radiation above Io's surface from Pele-type volcanic plumes and underground from the conduit wall. Proc. Lunar Planet. Sci. Conf. 34. Abstract 2123.

Zolotov, M.Y., Fegley, B., 2001. Chemistry and vent pressure of very high-temperature gases emitted from Pele volcano on Io. Proc. Lunar Planet. Sci. Conf. 32. Abstract 1474.